Provided for non-commercial research and education use.
Not for reproduction, distribution or commercial use.

This article appeared in a journal published by Elsevier. The attached copy is furnished to the author for internal non-commercial research and education use, including for instruction at the authors institution and sharing with colleagues.

Other uses, including reproduction and distribution, or selling or licensing copies, or posting to personal, institutional or third party websites are prohibited.

In most cases authors are permitted to post their version of the article (e.g. in Word or Tex form) to their personal website or institutional repository. Authors requiring further information regarding Elsevier's archiving and manuscript policies are encouraged to visit:

http://www.elsevier.com/copyright

Author's personal copy

Materials Science and Engineering R 61 (2008) 40–58

Contents lists available at ScienceDirect

Materials Science and Engineering R

journal homepage: www.elsevier.com/locate/mser

Stressed solid-phase epitaxial growth of ion-implanted amorphous silicon

N.G. Rudawski [a,*], K.S. Jones [a], R. Gwilliam [b]

[a] Department of Materials Science and Engineering, University of Florida, Gainesville, FL 32611-6400, United States
[b] Nodus Accelerator Laboratory, Advanced Technology Institute, Surrey Ion Beam Centre, Guildford, Surrey GU2 7XH, United Kingdom

ARTICLE INFO

Article history:
Available online 14 April 2008

Keywords:
Silicon
Amorphous
Stress
Strain
Solid-phase epitaxial growth
Ion-implantation

ABSTRACT

The kinetics of stressed solid-phase epitaxial growth (SPEG), also referred to as solid-phase epitaxy, solid-phase epitaxial regrowth, solid-phase epitaxial recrystallization, and solid-phase epitaxial crystallization, of amorphous (α) silicon (Si) created via ion-implantation are reviewed. The effects of hydrostatic, in-plane uniaxial, and normal uniaxial compressive stress on SPEG kinetics are examined in intrinsic (0 0 1)Si. Particular emphasis is placed on unifying the results of different experiments in a single-stress-dependent SPEG model. SPEG kinetics are observed to suffer similar exponentially enhanced growth rates in hydrostatic and normal uniaxial compressive stress. However, there are discrepancies between researchers in terms of the influence of in-plane stress on growth rates. Two different stress-dependent SPEG models are thus advanced, each with different physical bases. The model advanced by Aziz et al. proposes SPEG can be modeled as a single-atomistic process while the model advanced by Rudawski et al. suggests that stress influences the nucleation and migration processes of growth differently and that SPEG cannot be modeled as a single step. The basis for the Rudawski et al. model is based on the crystal island and ledge migration model of SPEG advanced by others. Morphological instabilities of the growing α/crystalline interface with in-plane compression are also addressed within the context of both the Aziz et al. and Rudawski et al. models. Finally, using the Rudawski et al. model, it is possible to examine, characterize, and isolate the different atomistic processes during growth. Calculation of the activation energies for nucleation and migrations processes suggests that the activation energy of 2.7 eV observed for the growth rate in stress-free SPEG by Olsen and Roth is representative of the activation energy for the single-atomistic process of crystal island nucleation. Thus, the study of stressed SPEG provides a new atomistic picture of the nature of growth.

© 2008 Elsevier B.V. All rights reserved.

Contents

1. Introduction . . . 41
2. The current understanding of SPEG . . . 41
   2.1. Important phenomena in SPEG . . . 41
   2.2. Transition state theory . . . 43
3. Experimental methods . . . 44
   3.1. Ion-implantation . . . 44
   3.2. Application of stress . . . 45
      3.2.1. Hydrostatic pressure . . . 45
      3.2.2. In-plane uniaxial stress . . . 45
      3.2.3. Normal uniaxial compression . . . 46
   3.3. Measurement of SPEG rates . . . 46
      3.3.1. Thin-film detection techniques . . . 46
      3.3.2. Site-specific FIB/XTEM method . . . 46
   3.4. Temperature calibration and annealing . . . 47

* Corresponding author. Tel.: +1 352 846 3353.
E-mail address: ngr@ufl.edu (N.G. Rudawski).

0927-796X/$ – see front matter © 2008 Elsevier B.V. All rights reserved.
doi:10.1016/j.mser.2008.02.002

Author's personal copy

4. Results and discussion . . . 47
4.1. Hydrostatic pressure . . . 47
4.2. In-plane uniaxial stress . . . 47
4.2.1. Early experiments . . . 47
4.2.2. Recent experiments . . . 49
4.3. Normal uniaxial compression . . . 52
4.4. Morphological istability . . . 53
4.5. Shortcomings of stress-dependent SPEG models . . . 53
4.6. Unification of earlier and recent stressed-SPEG results . . . 54
4.7. A new atomistic picture of SPEG . . . 54
5. Conclusions . . . 40
Acknowledgements . . . 40
References . . . 40

1. Introduction

Solid-phase epitaxial growth (SPEG) of amorphous (α) silicon (Si) created via ion-implantation and other non-equilibrium methods has been a phenomenon of fundamental and technological importance for several decades since being reported more than 50 years ago [1,2]. Much prior work has been devoted to understanding the energetics of the epitaxial α-Si to crystalline Si-phase transformation and the kinetics of the process. However, the impact of external stress on SPEG remains relatively unstudied and yet an important aspect to consider due to the ubiquitous nature of stresses during crystal growth processes in Si and other systems [3–10]. Therefore, this work is motivated not only by the large technological importance of SPEG of Si but by the goal to achieve a greater understanding of the influence of stress on solid–solid transformations and the atomistic nature of SPEG.

In the absence of any applied stress, the kinetics and macroscopic nature of SPEG of α-Si created via ion-implantation are well studied and understood. A schematic of the SPEG process is presented in Fig. 1. Basically, SPEG is the epitaxial growth process at an elevated temperature of a continuous α-Si layer in direct contact with a single-crystal Si substrate. The crystalline phase grows heterogeneously from the α/crystalline interface consuming the α-Si and results in a single crystal of Si. The process is also interchangeably referred to as solid-phase epitaxy, solid-phase epitaxial regrowth, solid-phase epitaxial crystallization, and solid-phase epitaxial recrystallization. Since SPEG of α-Si created via ion-implantation has been studied very extensively, many interesting phenomena are known about the process. However, though many studies have been conducted there is still very little understanding as to the atomistic nature of the growth process. A few models have been advanced, but none have been capable of explaining all issues pertaining to SPEG. Thus, though these issues are not all directly addressed here, it is partly the goal of this work to remain consistent within the prior work done by others.

Therefore, this works reviews the progress made in understanding the role of applied stress on SPEG kinetics. In particular, there is great emphasis on understanding the role of non-hydrostatic stresses on SPEG kinetics since non-hydrostatic stresses are prevalent during many crystal growth processes. Furthermore, new methods of applying non-hydrostatic stress and measuring SPEG kinetics have enabled greater and more detailed examination of stress-influenced SPEG. Unification between results from non-hydrostatic and hydrostatic stress experiments is also advanced. Ultimately, these studies provide a new atomistic picture of SPEG.

2. The current understanding of SPEG

2.1. Important phenomena in SPEG

The SPEG process in α-Si created via ion-implantation in the absence of stress has been extensively studied thus there are numerous different considerations that can influence the process. Most importantly, the SPEG rate is very temperature sensitive and displays classical Arrehnius-type behavior shown in Fig. 2 [11–13] which is given additional consideration in the following sections as it forms the basis for evaluating the influence of applied stress on growth kinetics. The SPEG kinetics of α-Si created via other methods are quite different and are not covered herein [13]. The introduction of impurities even in dilute concentrations can profoundly alter the growth kinetics. In the case of electrically active dopants such as boron, arsenic, and phosphorous (P), rate enhancements are observed as shown in Fig. 3 and this is generally

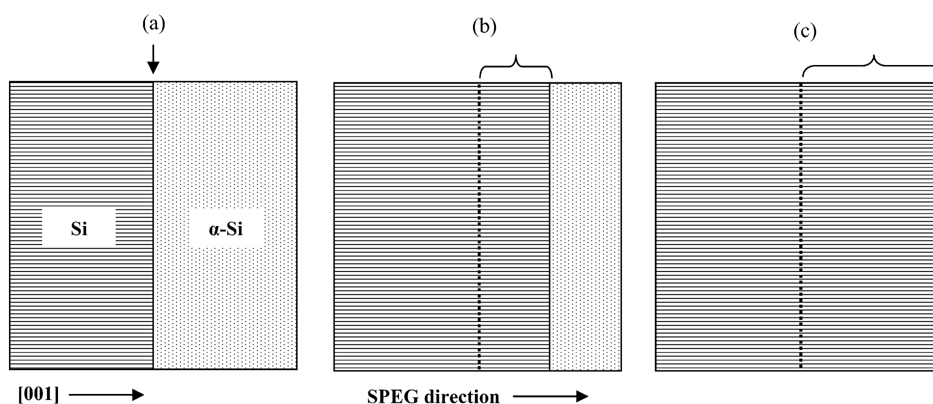

Fig. 1. Schematic of the SPEG process showing (a) the as-implanted state, (b) partial growth of an epitaxial Si layer, and (c) completed SPEG resulting in a single-Si crystal.

Author's personal copy

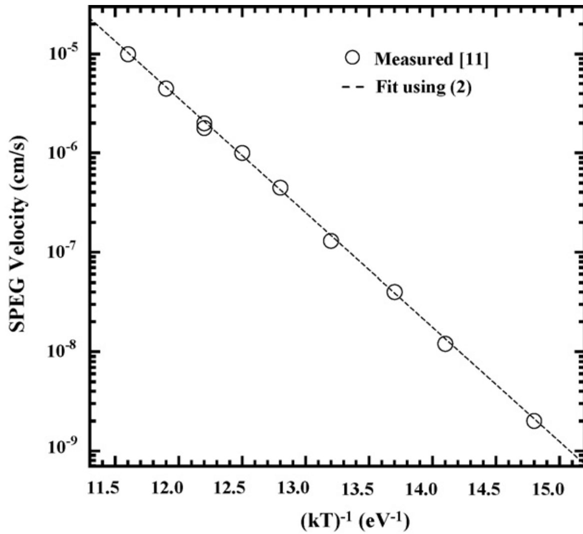

Fig. 2. Plot of SPEG velocity of vs. the reciprocal of kT as measured using TRR [11].

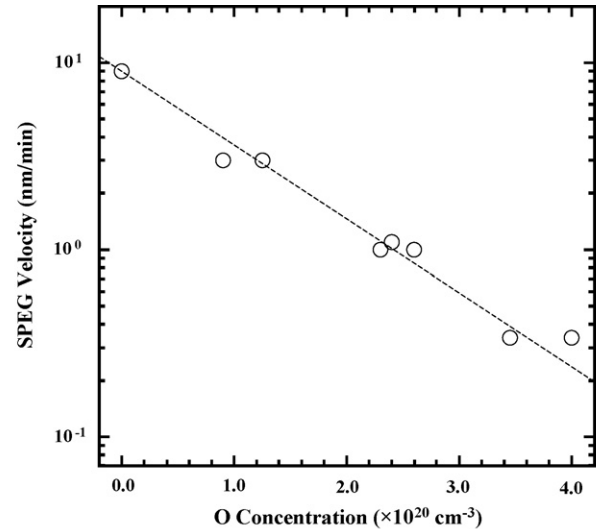

Fig. 4. Plot of SPEG velocity vs. O concentration at T = 550 °C as measured using RBS [18].

attributed to electronic processes occurring at the growing α/crystalline interface [14–17]. Non-dopant impurities such as hydrogen, nitrogen, carbon, and oxygen (O) tend to cause the opposite effect and retard the growth rate as presented in Fig. 4 [11,13,18]. Substrate orientation also drastically influences the growth kinetics. In particular, the velocity obeys a complex relationship with the misorientation angle of the substrate normal (θ) from [0 0 1] towards [1 1 0] with [1 1 1] growth nearly 25 times slower than [0 0 1] growth as displayed in Fig. 5 [19]. This is important to consider due to the technological importance of multi-directional growth in Si device processing [20–27].

It is important to note that the studies presented and reviewed herein are limited in scope to SPEG of intrinsic (0 0 1)α-Si created via ion-implantation since simultaneous consideration of stress influences with impurity/substrate orientation may be complicated. However, combined dopant, anisotropy, and stress effects during SPEG are technologically important and further investigation into these areas is warranted [28–35]. An excellent review of the different phenomena associated with stress-free SPEG of α-Si is presented by Olsen and Roth [13].

Many different atomistic models have been developed to explain the SPEG process. The earliest model was simple bond-rearrangement model developed by Csepregi et al. which was partially successful at predicting the substrate orientation dependence of SPEG [19]. Later, an interstitial-vacancy recombination model was developed by Narayan which was more successful at explaining the orientation dependence [36]. However, neither model was able to explain the impurity effects on SPEG. The latest and most accepted SPEG model advances that the growth process is mediated by the nucleation of crystal islands with subsequent island ledge migration in the growing α/crystalline interface [16,37,38]. The formation of a crystal island on an otherwise planar interface may be considered as a defect and thus this model is often referred to as the defect-mediation model of SPEG. This model is the most successful at explaining all the SPEG-related phenomena and requires greater examination as it forms the basis for explaining stress effects.

A schematic of the defect-mediated SPEG model is presented in Fig. 6. Small clusters of atoms rearrange to nucleate small crystalline islands one monolayer in height on the growing α/crystalline

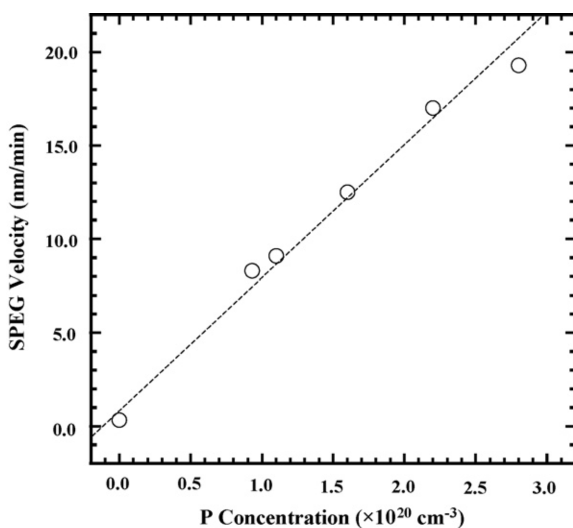

Fig. 3. Plot of SPEG velocity vs. P concentration at 475 °C as measured using RBS [15].

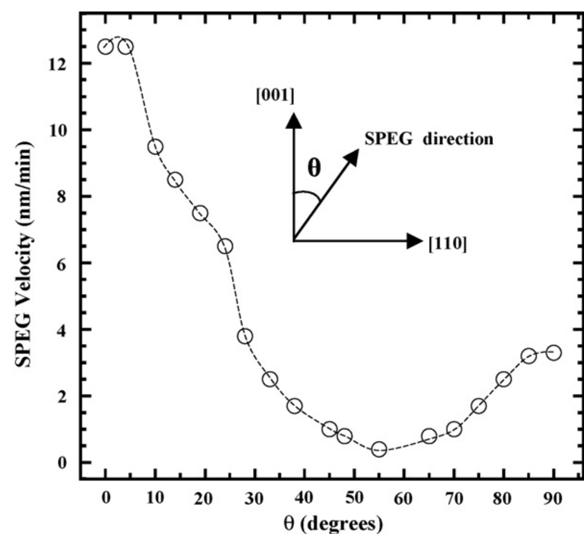

Fig. 5. Plot of SPEG velocity vs. θ at 550 °C as measured using RBS [19].

Author's personal copy

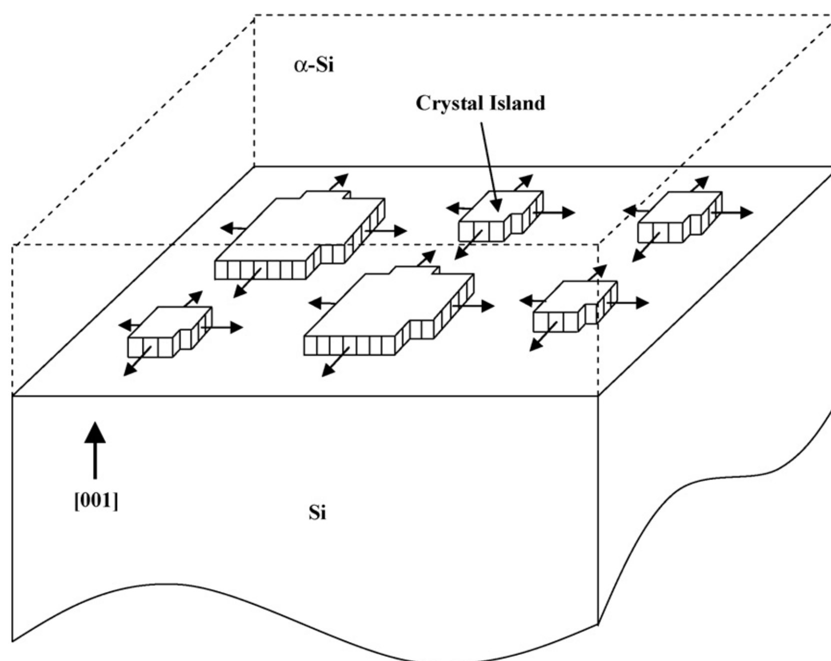

Fig. 6. Schematic of the defect-mediation model of [0 0 1]SPEG.

interface. The ledges of the island may be straight or have discontinuities. Atoms in the neighboring α-Si preferentially add to the crystal island at the ledges and kinks and propagate the islands laterally in the plane of the α/crystalline interface very rapidly. The process repeats once the monolayer is completed. It is not known if the ledges or kinks have preferred crystallographic orientations as plan-view investigation of SPEG is not possible though it was postulated that the edges of the islands would have ⟨1 1 0⟩ normals for (0 0 1) orientation [37,38]. However, it is not possible for SPEG on certain orientations to have ⟨1 1 0⟩ island edge normals since not all orientations contain ⟨1 1 0⟩ in-plane directions. Thus, some have advanced that island nucleation does not occur on some orientations and growth simply proceeds by atoms adding along the ⟨1 1 0⟩ direction(s) nearest the growth direction.

Unfortunately, ⟨1 1 0⟩ edge growth alone does not account for the well-known observation of highly defective SPEG of (1 1 1)Si. SPEG for this orientation typically is characterized by a high density of micro-twins and stacking faults [39–42]. The defects form as the result of atoms on the growing α/crystalline interface being incorrectly rotated about the growth direction which is also a bonding direction. Thus, if the atoms simply added along ⟨1 1 0⟩ edges, this would not occur. Therefore, crystal island nucleation appears to be an important process for all SPEG orientations.

Hence, two atomistic processes, nucleation and migration, both contribute to the SPEG rate and both must proceed for growth to occur. Thus, presumably, SPEG kinetics are limited by the slower of the two processes. In the absence of any stress, experiments by Williams et al. suggest the migration process is faster than the nucleation process [43]. Therefore, the nucleation rate is apparently limiting in the stress-free growth kinetics and the atomistic picture of SPEG can be explained by a single process to a first approximation. The model accounts for orientation-dependent SPEG since the nucleation and migration rates may differ between different α/crystalline interfaces. In the case of electrically active dopants, the rate of charged crystal islands at the growing α/crystalline interface is dramatically increased due to changes of the local Fermi level at the interface. In this model, non-dopant impurities do not alter the Fermi level and therefore alter the migration rates of the ledges by interfering with the α/crystalline interface arrangement. Dopant impurities presumably alter migration kinetics similarly to non-dopants. However, in the absence of impurity or orientation factors, it remains unknown what exact atomistic process is representative of the Arrhenius-type behavior of SPEG of α-Si created via ion-implantation. Moreover, the defect-mediated growth model has not been extended to explain stress-influenced SPEG.

2.2. Transition state theory

An Arrhenius-type process is that which has a rate, r, described by

$$r = r_0 \exp\left(\frac{-\Delta G^*}{kT}\right), \quad (1)$$

where r_0 is a temperature-independent pre-exponential factor, ΔG^* the activation energy for the process, k the Boltzmann's constant of 8.62×10^{-5} eV/K, and T is the absolute temperature as given in transition state theory (TST) [44]. The thermodynamics of the process are displayed schematically in Fig. 7. Thus, the system has free energy G_1 initially, arrives at a transition state with free energy, G^*, and then arrives at the final state with free energy G_2. Thus, $\Delta G^* = G^* - G_1$. Typically, the free energy difference between the initial and final states, given by $\Delta G_{1\text{-}2} = G_2 - G_1$ where G_2 is the free energy of the final state, negligibly impacts r provided $\Delta G_{1\text{-}2} < 0$ [13].

In the case of [0 0 1]SPEG of α-Si created via ion-implantation, ΔG^* is well known and characterized by activation energy of 2.7 eV and thus the velocity, v, of the advancing α/crystalline interface obeys a relationship analogous to (1) as presented in Fig. 2 and given by

$$v = v_0 \exp\left(\frac{-\Delta G^*}{kT}\right), \quad (2)$$

where v_0 is a temperature-independent pre-exponential factor [11–13]. The driving force for growth of the crystalline phase at the expense of the amorphous phase is a result of the free energy of the amorphous phase (the initial state) being higher than that of the crystalline state (the final state) [45,46]. Many solid–solid

Author's personal copy

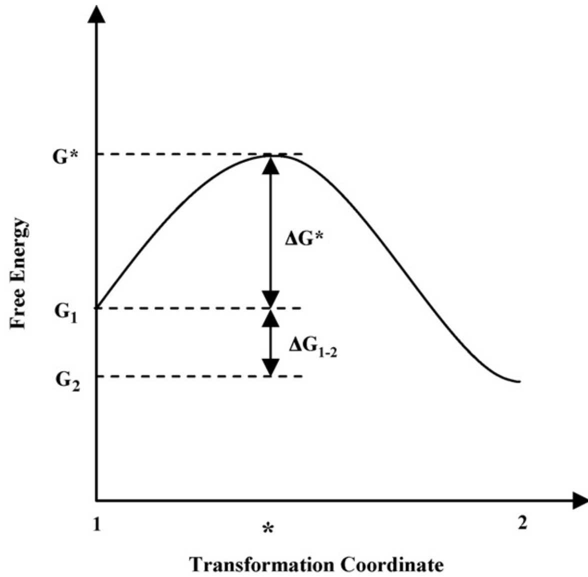

Fig. 7. Schematic of the energetics of a transformation between states 1 and 2.

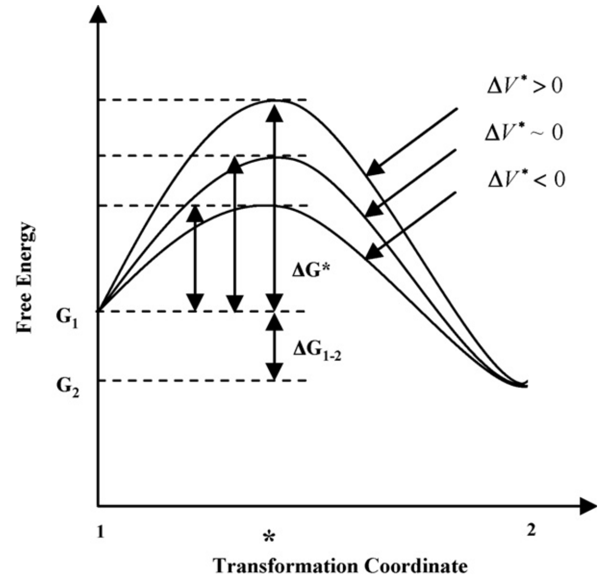

Fig. 8. Schematic of the energetics of a transformation between states 1 and 2 for different values of ΔV^* at high pressure.

transformations obey this type of relationship [47–50]. However, though ΔG^* = 2.7 eV is well known, it remains largely unknown what specific atomistic process or processes contributes to this term since the individual processes during growth have never been successfully isolated. A first guess might be to compare ΔG^* with the activation energies for point defect formation and migration in bulk Si. However, the activation term for SPEG is much different than the terms observed for point defect formation and nucleation in bulk Si [51]. Thus, it appears the SPEG process is composed of unique atomistic processes not found in bulk Si.

The addition of external hydrostatic pressure can profoundly change r given in (1). Thus, ΔG^* at constant hydrostatic pressure can be expanded to

$$\Delta G^* = \Delta U^* + P_0 \Delta V^* - T\Delta S^*, \tag{3}$$

where ΔU^* is the change in internal energy, P_0 the hydrostatic pressure initially (normal atmospheric pressure), ΔV^* the change in volume, and ΔS^* is the change in entropy between the initial and transition states. If the pressure is changed to P, ΔG^* becomes ΔG_1^* as given by

$$\Delta G_1^* = \Delta U^* + P\Delta V^* - T\Delta S^*. \tag{4}$$

Thus, if P is much greater than P_0 (very often the case in situations of externally applied stress), the new activation barrier for the rate of the process is nearly equivalent to $P\Delta V^* + \Delta G^*$ and r is given by

$$r = r_0 \exp\left(\frac{-P\Delta V^* - \Delta G^*}{kT}\right). \tag{5}$$

Thus, more specifically

$$\Delta V^* = -kT\frac{\partial \ln(r)}{\partial P}. \tag{6}$$

Depending on the sign of ΔV^*, the activation barrier will be increased or decreased as presented in Fig. 8. The application of pressure can also influence the free energy difference between initial and final states. However, provided the driving force for growth is still present, the activation barrier typically still has the greatest influence on growth kinetics. In reality, the applied stress state, σ_{ij}, can be more complicated than simple hydrostatic pressure and the change in volume can be represented using the activation strain tensor, ΔV_{ij}^*, which is the volumetric deformation between the initial and transition states [52]. Thus, in the most general case, (5) is represented by

$$r = r_0 \exp\left(\frac{\sigma_{ij}\Delta V_{ij}^* - \Delta G^*}{kT}\right) \tag{7}$$

and the most general form of ΔV_{ij}^* is given by

$$\Delta V_{ij}^* = kT\frac{\partial \ln(r)}{\partial \sigma_{ij}}. \tag{8}$$

Hence, a positive (negative) $\sigma_{ij}\Delta V_{ij}^*$ product decreases (increases) the activation barrier. Thus, it is this TST argument that provides the majority of the basis for explaining the influence of stress on SPEG kinetics. Due to the strong Arrhenius behavior of the stress-free SPEG velocity, it is very tempting to assume SPEG is regulated by a single-atomistic process and combine (2) and (7) and predict $\Delta V_{ij}^* = kT\,\partial \ln(v)/\partial\sigma_{ij}$ can be used to describe stress-induced changes to growth kinetics. However, experiments suggest SPEG is composed of both nucleation and migration processes and this becomes important to consider when trying to explaining some of the phenomena observed with stress-induced changes to growth kinetics.

3. Experimental methods

3.1. Ion-implantation

In this study, the generation of continuous α-Si films on Si substrates was effected via Si^+-implantation at vacuum of $\sim 8 \times 10^{-8}$ Torr into single-crystal 50-μm thick polished impurity-free (0 0 1)Si substrates. Due to the high vacuum used for implantation, it is reasonably assumed that the amounts of any unintentional impurities implanted were negligible. No other species were used for amorphization since impurities tend to profoundly alter the growth kinetics in the absence of any stress and this complication needed to be avoided. All Si^+-implantation was conducted at room temperature in a vacuum ambient using a commercial ion-implantation system. A chain of implants with energies of 50, 100, and 200 keV to doses of 1×10^{15}, 1×10^{15}, and 3×10^{15} cm^{-2}, respectively, generated an α-Si layer ~350-nm thick with high repeatability. The resulting film thickness was

Author's personal copy

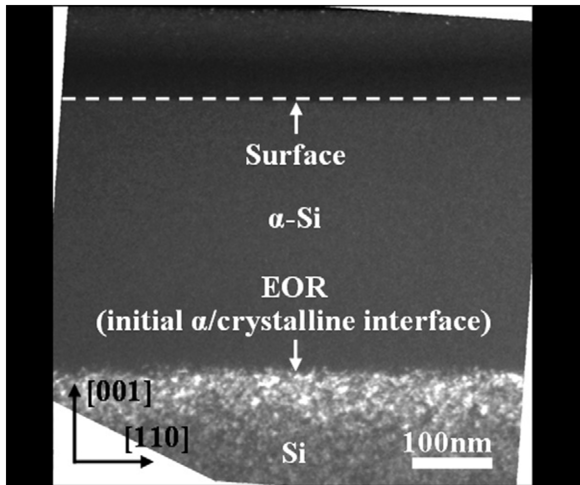

Fig. 9. WBDF-XTEM image of a typical as-implanted α-Si layer used for measurement of SPEG kinetics.

approximately the value predicted by simulations [53]. A weak-beam dark-field cross-sectional transmission electron microscopy (WBDF-XTEM) image of a typical as-implanted specimen is shown in Fig. 9. A band of defective Si near the end of range (EoR) of the implantation process is observed in the crystalline region just beyond the initial α/crystal interface. Upon annealing, this region evolves into extended defects which have been thoroughly studied in the literature [54]. Since the EoR defects form away from the growing α/crystalline interface, it is accepted that no influence from the EoR on SPEG kinetics exists. Other studies of stressed SPEG also utilized Si^+-implantation into single-crystal (0 0 1)Si for amorphization, but the implantation energies, doses, and substrate temperatures were typically different. It is not believed that differences in the implant conditions may have influenced the results of any experiments since the implanted species was always Si.

3.2. Application of stress

3.2.1. Hydrostatic pressure

A schematic of an α/crystalline interface growing with hydrostatic pressure, σ, is presented in Fig. 10(a). Various different devices have been used for inducing hydrostatic pressure at elevated temperatures by other researchers. Diamond anvil cells and cylinder piston presses are the most common and are described elsewhere [55–57]. Typically, hydrostatic pressures up to 5.0 GPa are easily attainable with these devices. Some also allow for in situ monitoring of SPEG.

3.2.2. In-plane uniaxial stress

A schematic of an α/crystalline interface growing with in-plane uniaxial stress, σ_{11}, is presented in Fig. 10(b). The experimental apparatus used to induce and measure uniaxial stress in the Si wafers is presented in Fig. 11. The wafers were cleaved along the in-plane ⟨1 1 0⟩ directions into elongated strips with approximate dimensions of ~0.2 cm × 1.8 cm and then bent by hand along the elongated direction and the ends of the strips inserted into slots in a quartz tray spaced ~1.5 cm apart. Thus, the strip is self-supported by the normal force from the quart tray. A classical beam-bending argument suffices to determine the in-plane stress at point x on the wafer surface, $\sigma_{11}(x)$, where x is the lateral coordinate on the bent wafer surface with $x = 0$ taken to be the apex of the bent wafer. For a wafer with uniaxial stress generated by bending, $\sigma_{11}(x)$ is given by

$$\sigma_{11}(x) = \frac{E_{[1\,1\,0]}c}{r(x)}, \quad (9)$$

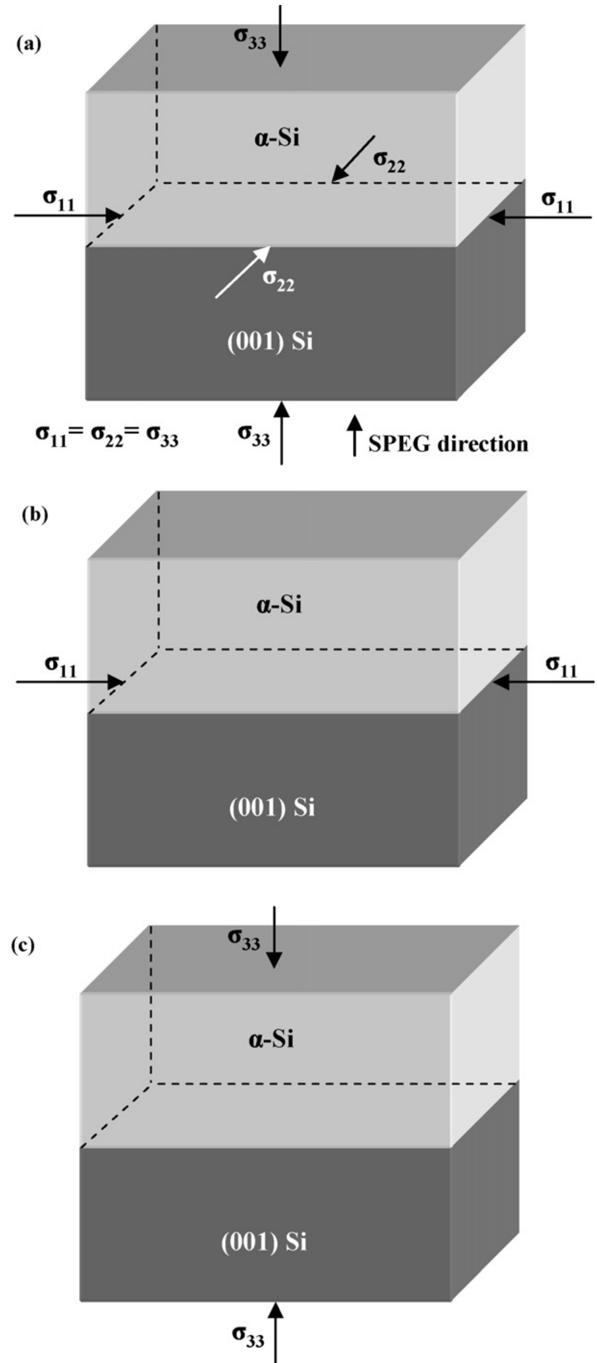

Fig. 10. Schematics of the [0 0 1]SPEG process occurring with (a) hydrostatic stress, (b) in-plane uniaxial stress, and (c) normal uniaxial compressive stress.

where $E_{[1\,1\,0]}$ is the [1 1 0] Young's modulus of Si [50], c the wafer half-thickness (25 μm), and $r(x)$ is the local radius of curvature at point x on the wafer surface [58,59]. By convention, the 1 and 2 directions are the in-plane directions and 3 is the wafer normal (growth) direction. At x on the top of the strip the stress state is uniaxial tension while on the bottom the stress state is uniaxial compression of equal magnitude. The value of $E_{[1\,1\,0]}$ does show some slight variability over the temperature range of 500–600 °C and this was accounted for in the stress calculations [60]. Determination of $r(x)$ was accomplished via the use of a Philtec laser displacement sensor system. The laser system was translated over the surface of the bent wafer to determine the deflection (y) of the wafer from the tip of the laser sensor at a given x coordinate.

Author's personal copy

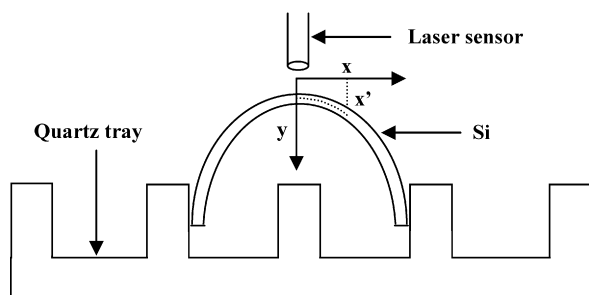

Fig. 11. Schematic of the apparatus used to induce and measure in-plane uniaxial stress in Si wafers.

Thus, a discrete set of coordinates was obtained which allowed the surface of the wafer to be fit to a mathematical function $y = y(x)$. In all cases, a parabola was a very decent fit to the coordinates. Thus, $r(x)$ is given by

$$\frac{1}{r(x)} = \frac{\mathrm{d}^2y(x)/\mathrm{d}x^2}{(1+(\mathrm{d}y(x)/\mathrm{d}x)^2)^{3/2}} \tag{10}$$

and $\sigma_{11}(x)$ can be determined. Maximum repeatable stresses of 1.3 ± 0.1 GPa were attained. Once the strips were removed from the bending apparatus, the x coordinate was transformed into the corresponding unbent displacement, x', by computing the arc length of the bent strip as given by

$$x' = \int_0^a \left(1 + \left(\frac{\mathrm{d}y(x)}{\mathrm{d}x}\right)^2\right)^{1/2} \mathrm{d}x, \tag{11}$$

where a is the lateral displacement from the apex of the bent wafer.

It is important to note that even though Si is very brittle at room temperature [61,62], plastic deformation of crystalline Si can occur given prolonged annealing at temperatures used in this study given sufficient stress and this can cause stress relaxation [63–65]. However, upon removal from the bending apparatus, the strips did not exhibit any detectable curvature suggesting no appreciable stress–relaxation occurred. Also, α-Si does exhibit some viscoelastic behavior which may give rise to flow of the amorphous phase with stress [66,67]. However, no detectable flow of α-Si was observed since the surface–EoR distance did not change measurably in any samples.

Other researchers have used wafer-bending techniques to induce uniaxial stress during SPEG [52,59]. Four-point and three-point bending apparatuses capable of inducing stresses to 0.6 GPa in 750-μm thick wafers were used. Analysis of the stress state is much easier in this case compared to self-supported bending, but suffers from the lower range of stresses attainable due to the lower fracture toughness of thicker Si wafers [68–72].

3.2.3. Normal uniaxial compression

A schematic of a growing α/crystalline interface with normal uniaxial compression, σ_{33}, is displayed schematically in Fig. 10(c). A high-temperature piston/cylinder apparatus was used by Barvosa-Carter to induce normal uniaxial compression at temperatures sufficient to affect SPEG. To date, this has been the only study of normal uniaxial compression effects on SPEG. The apparatus is described elsewhere [73].

3.3. Measurement of SPEG rates

3.3.1. Thin-film detection techniques

In prior studies of SPEG kinetics by other researchers, velocity data was collected in situ via the use of time-resolved reflectivity (TRR) measurements, Rutherford backscattering (RBS), and other thin-film techniques [11–13,18,19,52,74–76]. These techniques provide large amounts of growth data for determination of the growth rates. However, such analysis techniques are not highly site specific and this poses problems when a continuous and large stress gradient exists in the specimens as is the case in some of the presented studies. Furthermore, any morphological instability in the growing α/crystalline interface cannot be accounted for in thin-film detection techniques as such methods are susceptible to averaging of data and provide little structural information. Roughening of the growth fronts can also reduce the accuracy of rate measurements using thin-film detection techniques.

3.3.2. Site-specific FIB/XTEM method

Focused ion beam (FIB) milling with an FEI Strata DB235 dual focused ion beam/scanning electron microscope utilizing a gallium (Ga) ion beam accelerated to 30 keV was used to prepare samples for WBDF-XTEM imaging with a g_{220} two-beam condition using a JEOL 200CX transmission electron microscope. Specimens were prepared at different anneal times and stresses and the α-Si thickness as a function of time was thus measured using WBDF-XTEM for a given stress and the SPEG velocity estimated using standard least squares regression techniques. The surface to α/crystalline front distance was chosen for rate measurements due to the crisp and sharp nature of the two interfaces. The algorithm for measuring growth in WBDF-XTEM images used ImageJ© analysis software to trace the sample surface and resulting α/crystalline interface after annealing into finely discretized sets of coordinates for several different images. An example of this process is shown in Fig. 12 Then, the average resulting α-Si thickness was calculated along with the root-mean-squared roughness (R_{RMS}) of the resulting growth front. Thus, all reported errors in α-Si thickness measurements are given as R_{RMS}. A typical plot of α-Si thickness versus time is shown in Fig. 13.

This method affords the distinct advantage that FIB sample preparation is very site specific. The samples generated were typically ~10 μm long or less and thus it may be reasonably concluded that the stress was uniform through the whole of the samples thus avoiding the complication of an intra-sample stress gradient. Furthermore, using WBDF-XTEM for the thickness measurements affords advantages in terms of spatial resolution and detailed structural knowledge of the evolving α/crystalline interface. Additionally, it is not believed that FIB preparation caused any appreciable specimen damage since all specimens were coated with carbon and platinum layers of sufficient thickness prior to milling to prevent Ga^+-implantation as predicted by simulations [53]. The main disadvantage of this method is that it is not an in situ technique and requires discretization of the growth process. Therefore, using this method it is difficult to detect any

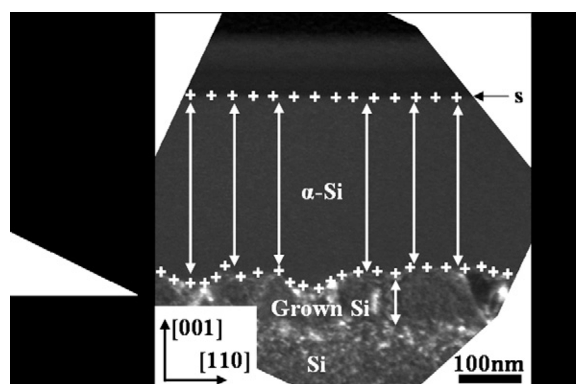

Fig. 12. WBDF-XTEM image of an annealed specimen showing the process used to measure the resulting α-Si thickness. The surface (indicated by 's') and resulting α/crystalline interface after growth are discretely represented (+) with the arrows representing α-Si thickness variations within the image.

Author's personal copy

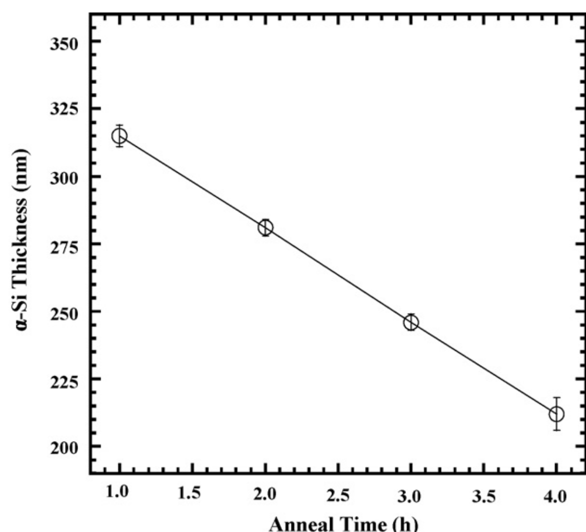

Fig. 13. Typical plot of α-Si thickness vs. time generated by annealing different specimens for different anneal times as measured using WBDF-XTEM.

temporal dependence of the growth rate which may arise. However, for the case of impurity-free (0 0 1)Si, the growth rate as measured using in situ techniques has never shown any significant variability with time once the specimens reach thermal equilibrium and a few nm of growth has occurred beyond the initial α/crystalline interface [13]. The plot shown in Fig. 13 reflects this since there is very little observed variability in v with annealing time. Thus, it is reasonably assumed that the growth kinetics do not vary with time.

3.4. Temperature calibration and annealing

Due to the ex situ nature of the experiments, the anneal temperature, T, was not obtained during SPEG as it was in previous in situ studies. In this study, the quartz tray apparatus was inserted into a tube furnace used for annealing and allowed to come to thermal equilibrium with the furnace. The position of the tray in the tube furnace was kept constant for all anneals. Then a thermocouple was placed on the middle of the tray and carefully manipulated so as not to touch any other part of the tray or the inside of the tube. It was at this position on the tray that tensile, compressive, and stress-free specimens (three unique wafer strips) were annealed simultaneously for each time and temperature. Thus, the error in all T measurements was estimated at ±1 °C. A schematic of the annealing setup used is presented in Fig. 14. Nitrogen (N_2) ambient was used for all annealing as well as for temperature measurements. For these studies, T = 500–575 °C was used with anneal times of 0.3–7.5 h. The quartz tray was inserted at room temperature into the pre-calibrated furnace and reached equilibrium with the furnace very quickly (<2 min). Thus, since the ramp-up time to reach equilibrium was much smaller than any of the anneal times it is assumed that the specimens were given isothermal processing.

4. Results and discussion

4.1. Hydrostatic pressure

The effect of stress on SPEG kinetics was first examined under hydrostatic pressure [76–80]. A plot of α/crystalline interface displacement versus time at 500 °C at various levels of hydrostatic pressure as measured using RBS is presented in Fig. 15 [76]. For each value of pressure, the SPEG rate appears linear with time and the rate is enhanced with pressure. A plot of SPEG rates extracted from Fig. 15 versus pressure is shown in Fig. 16 [76]. The data suggests the SPEG rate is exponentially pressure dependent. Thus, v takes the stress-dependent form

$$v = v(0)\exp\left(\frac{\Delta V_h^*\sigma}{kT}\right), \tag{12}$$

where σ is the hydrostatic stress, ΔV_h^* the activation volume in hydrostatic pressure of −0.75 Ω, and $v(0)$ is the stress-independent SPEG velocity at T, where Ω is the atomic volume of Si [76]. Thus, as per (7), the SPEG velocity under hydrostatic stress is accurately modeled using TST assuming a single-atomistic growth process. Later experiments of hydrostatic pressure-enhanced SPEG measured using TRR revealed results similar to the earlier experiments. A plot of SPEG rate versus σ for T = 520–550 °C is shown in Fig. 17 [78]. The rates exhibit similar pressure enhancement with stress at all three temperatures and $\Delta V_h^* = (-0.28 \pm 0.03)\Omega$ [77,78]. The difference in the activation volume terms is unclear, though it was postulated that the stress state employed by Nygren et al. may have been significantly deviant from true hydrostatic pressure [76]. The measurement techniques were also different [76,78].

These early hydrostatic pressure experiments were instrumental in determining the importance of the transition state in SPEG kinetics. Moreover, it suggested that the SPEG process could be explained as being the result of a single-atomistic process or dominated by a single-atomistic process. However, as per the defect-mediated model of SPEG, it was unclear which atomistic process was being altered via application of hydrostatic stress or if the defect-mediation model could explain the compelling results. However, the study of non-hydrostatic stresses on SPEG kinetics would eventually resolve this in subsequent experiments.

4.2. In-plane uniaxial stress

4.2.1. Early experiments

Aziz et al. were the first to investigate the influence of non-hydrostatic stresses on SPEG kinetics in α-Si created via ion-implantation [52]. They applied uniaxial stress in the plane of the growing α/crystalline interface, σ_{11}. A clever method of sample preparation implanted both sides of the wafer strips so that compressive and tensile specimens were annealed simultaneously on each strip. Three-point bending was used to induce stress.

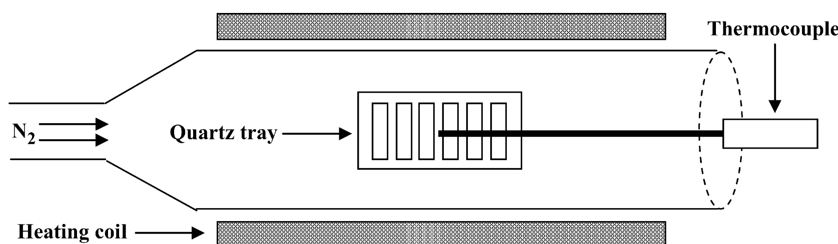

Fig. 14. Schematic of the apparatus used for annealing and temperature calibration.

Author's personal copy

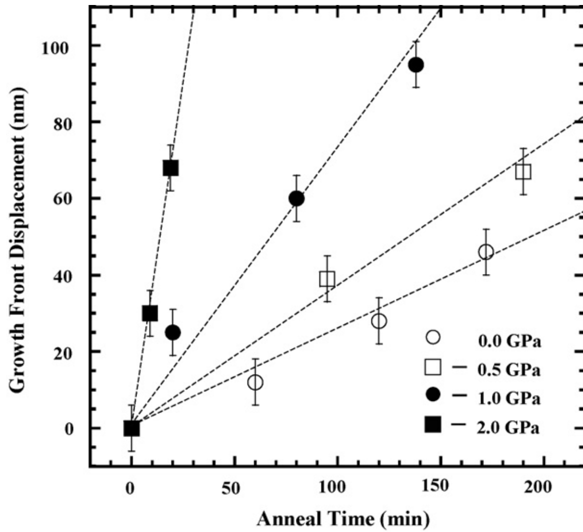

Fig. 15. Plot of α/crystalline interface displacement vs. time for different σ at 500 °C as measured using RBS [76].

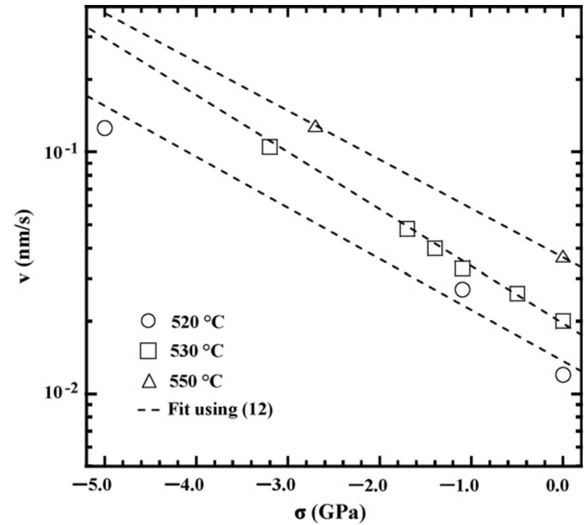

Fig. 17. Plot of SPEG velocity vs. σ for different T as measured using TRR [78].

Fig. 18 is a plot of the SPEG rate at 540 °C measured using RBS versus displacement from the strip centers for different samples. The maximum stress occurs at mid-strip with a linear stress gradient outward to 10 mm either side of center at which point $\sigma_{11} = 0$. The stresses indicated in Fig. 18 are indicative of σ_{11} at the center of the strips (maximum stress). For each strip, the tensile side of the strip had faster growth rates than the compressive side at the corresponding lateral displacements. In general, Fig. 18 also suggests that $\sigma_{11} > 0$ causes SPEG enhancement and $\sigma_{11} < 0$ causes retardation. Fig. 18(a) and (b) suggest that tension causes SPEG enhancement with compression not significantly altering the stress-free rate. However, Fig. 18(c) shows a much different trend, with tension not significantly altering the stress-free rate and compression causing larger retardation.

Fig. 19 presents a plot of the normalized SPEG rate versus σ_{11} with the data presented in Fig. 18. The overall trend in the data does show enhancement to the SPEG rate in tension and retardation in compression. However, there are many inconsistencies within this trend, especially near the vicinity of $\sigma_{11} = 0$ where the growth rates show large amounts of variation.

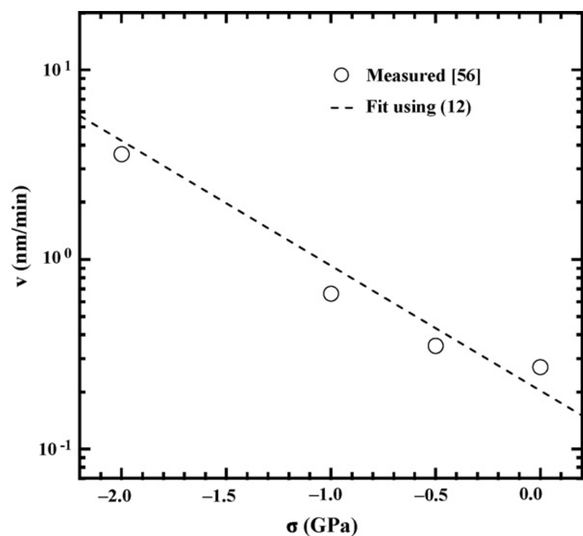

Fig. 16. Plot of SPEG velocity vs. σ at 500 °C as measured using RBS [76].

Most interestingly, the observations of uniaxial stress are strikingly different than those of hydrostatic stress. Most notably, uniaxial compression causes retardation where as hydrostatic pressure causes enhancement. However, the data seem to obey a relationship similar to (7) and (12) given by

$$v = v(0)\exp\left(\frac{\Delta V_{11}^{*}\sigma_{11}}{kT}\right), \quad (13)$$

where $\Delta V_{11}^{*} = (0.15 \pm 0.01)\Omega$ is the in-plane activation volume for SPEG. This data is consistent with the observations of hydrostatic stress in that stress-induced changes to SPEG can be accurately modeled with TST as a single-atomistic step. Thus, unification of the hydrostatic pressure experiments [76–80] reveals

$$\Delta V_{\mathrm{h}}^{*} = 2\Delta V_{11}^{*} + \Delta V_{33}^{*} \quad (14)$$

since the in-plane terms must be equal due to symmetry constraints for (0 0 1)Si, again assuming SPEG is governed by a single-atomistic process. Therefore, using $\Delta V_{\mathrm{h}}^{*} = (-0.28 \pm 0.03)\Omega$, ΔV_{ij}^{*} has the form

$$\Delta V_{ij}^{*} = \begin{pmatrix} 0.15 & 0 & 0 \\ 0 & 0.15 & 0 \\ 0 & 0 & -0.58 \end{pmatrix}\Omega. \quad (15)$$

This model provides unification between hydrostatic pressure-enhanced SPEG results and the results from in-plane uniaxial stress in early experiments. The specific values in (15) suggest that the transition state involves an in-plane biaxial expansion and normal contraction. The trace of (15) being negative may be indicative of the density of crystalline Si being greater than that of the amorphous counterpart [81]. It was proposed that in-plane expansion enhances SPEG by opening the growth interface and allowing easier atomic motion [54]. However, it is important to once again note that this model assumes the two atomistic processes of nucleation and migration can be modeled as a single-atomistic process in terms of stress-influenced SPEG. More specifically, this implies

$$\Delta V_{ij}^{*} = \Delta V_{ij}^{\mathrm{n}} + \Delta V_{ij}^{\mathrm{m}}, \quad (16)$$

where $\Delta V_{ij}^{\mathrm{n}}$ and $\Delta V_{ij}^{\mathrm{m}}$ are the nucleation and migration strain tensors associated with arriving at the transition state.

Author's personal copy

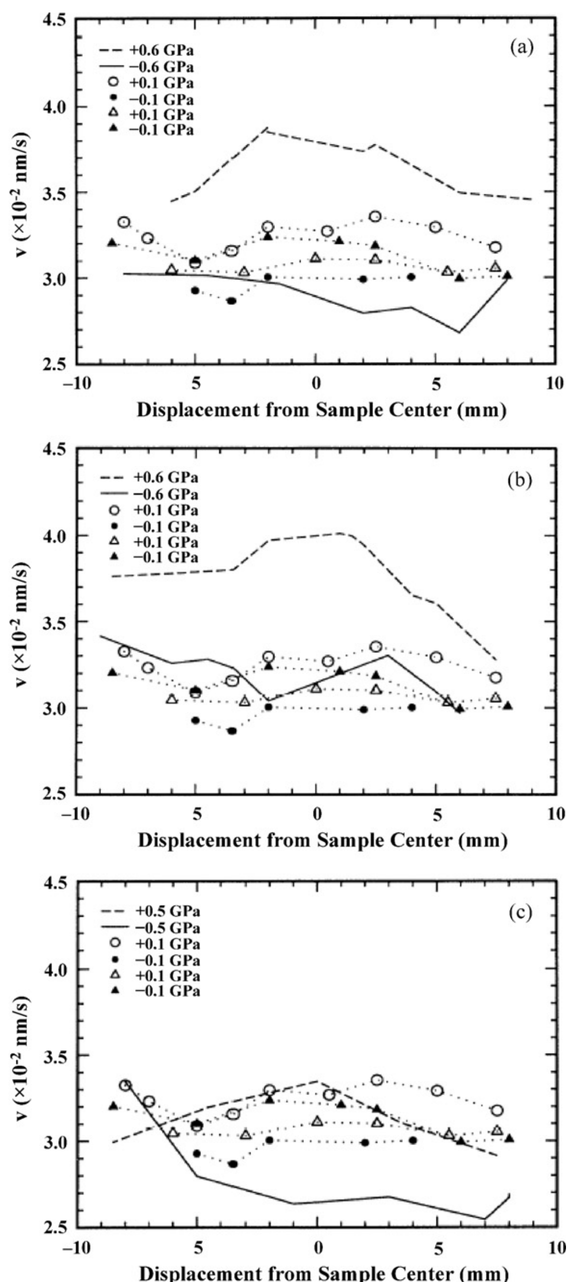

Fig. 18. (a)–(c) Plots of SPEG velocity vs. displacement from the center of several different specimens in three-point bends at 540 °C as measured using RBS. The stresses indicated correspond to the maximum magnitude of σ_{11} induced in the pieces at zero displacement [52]. In all cases, (—) and (– – –), (○) and (●), and (△) and (▲) correspond to the tensile and compressive sides of the same wafer strips, respectively. Reproduced and modified with permission from M.J. Aziz, P.C. Sabin, G.-Q. Lu, Phys. Rev. B. 44 (18) (1991) 9812. Copyright (1991) by the American Physical Society.

Subsequent experiments of non-hydrostatic in-plane uniaxial compression on SPEG of α-Si revealed consistent results with the initial work of Aziz et al. [82–84]. In a similar system, SPEG of strained silicon–germanium (SiGe) on Si showed that compressive biaxially stressed SiGe grew much slower than the relaxed counterpart [85–87]. In this case, the activation volume for in-plane biaxial stress was estimated to be 0.34 Ω, close to twice that of ΔV_{11}^{*} which is near the expected result. However, the case of tension was not evaluated in the same SiGe system and thus it remained unknown if the activation volume was consistent within all stress states. Additionally, the introduction of Ge can profoundly alter the growth kinetics in unstrained material and this may be a complicating effect making the results from SiGe experiments difficult to compare with Si experiments [88]. Thus, the results from strained-SiGe experiments appear to corroborate the work by Aziz et al., but suffer from the lack of isolation of Ge and stress effects.

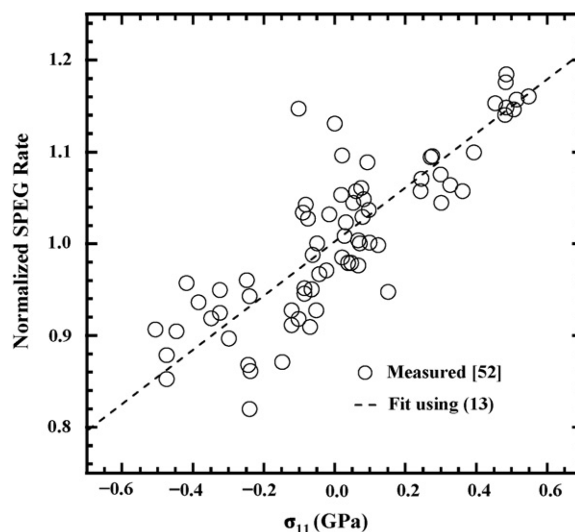

Fig. 19. Plot of normalized SPEG rate vs. σ_{11} at 540 °C as measured using RBS [52].

4.2.2. Recent experiments

A series of recent experiments studied the same basic system that Aziz et al. investigated over 15 years prior [89]. However, the method of applying in-plane uniaxial stress was that presented in Section 3.2.2 and thus the range of stresses was much greater than the earlier experiments.

Fig. 20(a) presents a WBDF-XTEM of an as-implanted specimen for reference. After annealing for 4.0 h at 525 °C without stress, shown in Fig. 20(e), 138 ± 6 nm of growth occurred [89]. For in-plane compression with σ_{11} = −0.5, −1.0, and −1.3 GPa, shown in Fig. 20(b)–(d), 77 ± 9, 72 ± 8, and 68 ± 9 nm of growth occurred, indicative of SPEG retardation [89]. There is interfacial roughening of the α/crystalline interface in compression which is given additional consideration in a subsequent section. Regarding in-plane tension cases of σ_{11} = 0.5, 1.0, and 1.3 GPa, shown in Fig. 20(f) and (g), 138 ± 6 nm of growth occurred which is similar to stress-free case [89].

Annealing of specimens for 1.0, 2.0, and 3.0 h was performed for all values of stress and the resulting amounts of growth measured using WBDF-XTEM as presented in Fig. 21. From this data, v versus σ_{11} was calculated as presented in Fig. 22. No detectable difference was observed in v for $0 \leq \sigma_{11} \leq 1.3$ GPa with an SPEG rate of 34 ± 2 nm/h. In compression, v was retarded to a limiting rate of 17 ± 2 nm/h for $-1.3 \leq \sigma_{11} \leq -0.5$, while $\sigma_{11} = -0.25$ GPa caused retardation to 22 ± 2 nm/h. The behavior of v predicted by Aziz et al. is provided for comparison [52]. There was no change in the SPEG rate for tension though the Aziz et al. model predicts enhancement. However, the retardation in compression is consistent with the model and prior work [52,82–84]. Interestingly, in compression, v appears to reach a limiting value and the rates show large deviations from the Aziz et al. predictions [52].

It appears that the recent results [89] cannot be reasonably explained by the Aziz et al. model of stressed SPEG and thus it becomes necessary to consider a new model to explain the data [52]. A good starting point is the groundbreaking study of

Author's personal copy

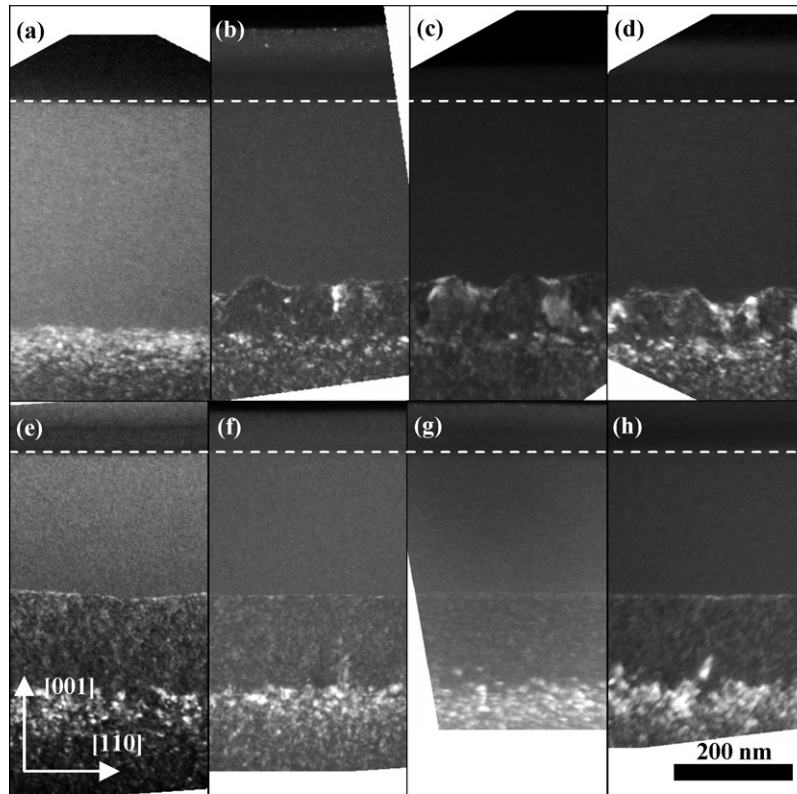

Fig. 20. (a) WBDF-XTEM image of an as-implanted specimen. WBDF-XTEM images of specimens annealed at 525 °C for 4.0 h with different values of σ_{11}: (b) −0.5 GPa, (c) −1.0 GPa, (d) −1.3 GPa, (e) 0 GPa, (f) 0.5 GPa, (g) 1.0 GPa, and (h) 1.3 GPa [89]. Reproduced and modified with permission from N.G. Rudawski, K.S. Jones, R. Gwilliam, Phys. Rev. Lett. in press (2008). Copyright (2008) by the American Physical Society.

Williams et al. which revealed the importance of nucleation and migration processes in SPEG kinetics [43]. The rate of island nucleation, τ_{n}^{-1}, is a scalar property while the rate of ledge migration for a generalized α/crystalline interface, $\tau_{\text{m},ij}^{-1}$, is a second order tensor property analogous to diffusivity or mobility given in expanded form by

$$\tau_{\text{m},ij}^{-1} = \begin{pmatrix} \tau_{\text{m},11}^{-1} & \tau_{\text{m},12}^{-1} \\ \tau_{\text{m},21}^{-1} & \tau_{\text{m},22}^{-1} \end{pmatrix}. \tag{17}$$

In the case of the α-Si/(0 0 1)Si interface without any stress, (17) reduces to

$$\tau_{\text{m},ij}^{-1} = \begin{pmatrix} \tau_{\text{m},11}^{-1} & 0 \\ 0 & \tau_{\text{m},11}^{-1} \end{pmatrix} \tag{18}$$

as the result of symmetry constraints. Thus, the velocity of ledge migration, $v_{\text{m},i}$, in expanded form is given by

$$\begin{pmatrix} v_{\text{m},1} \\ v_{\text{m},2} \end{pmatrix} = \begin{pmatrix} \tau_{\text{m},11}^{-1} & 0 \\ 0 & \tau_{\text{m},11}^{-1} \end{pmatrix} \begin{pmatrix} \Delta x_1 \\ \Delta x_2 \end{pmatrix}, \tag{19}$$

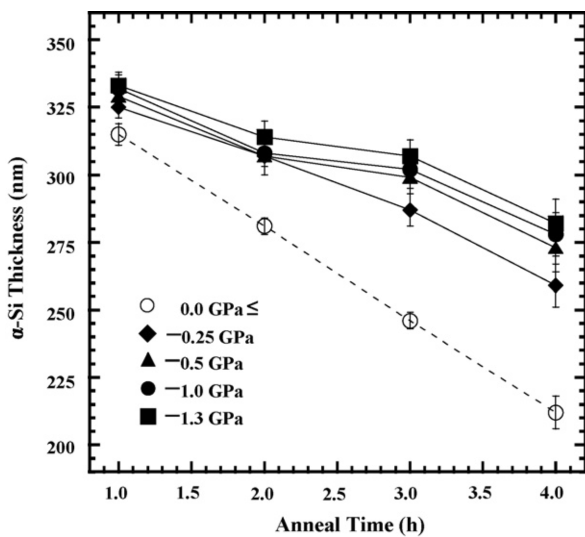

Fig. 21. Plot of α-Si thickness vs. annealing time at 525 °C for different values of σ_{11} as measured using WBDF-XTEM.

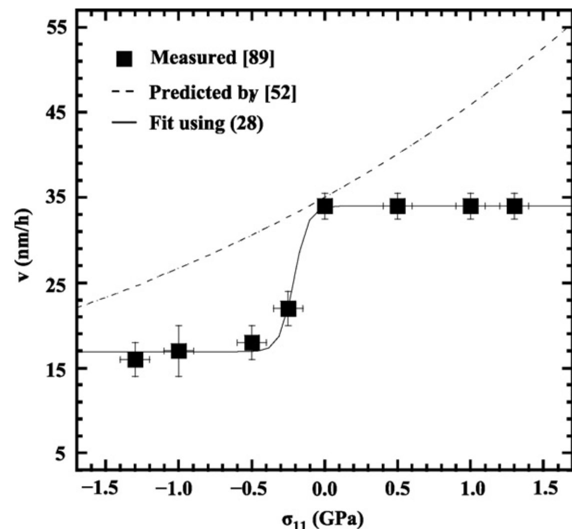

Fig. 22. Plot of v vs. σ_{11} at 525 °C as measured using WBDF-XTEM [89]. Reproduced with and modified with permission from N.G. Rudawski, K.S. Jones, R. Gwilliam, Phys. Rev. Lett. in press (2008). Copyright (2008) by the American Physical Society.

Author's personal copy

where Δx_j is the ledge migration vector dependent on the crystallography of the α/crystalline interface and the coordinate frame of reference. Both $v_{m,1}$ and $v_{m,2}$ contribute to the overall growth velocity and are presumably independent of one another. The nucleation of crystal islands with monolayer thickness Δx (0.14 nm) causes additional contribution to the overall growth rate. However, it is necessary to take into account that both nucleation and migration processes must be accomplished for growth to proceed. Thus, v is given by

$$v = \frac{1}{1/(\tau_n^{-1}\Delta x) + 1/(v_{m,1})} + \frac{1}{1/(\tau_n^{-1}\Delta x) + 1/(v_{m,2})}, \quad (20)$$

which further reduces to

$$v = \frac{1}{1/(\tau_n^{-1}\Delta x) + 1/(\tau_{m,11}^{-1}\Delta x_1)} + \frac{1}{1/(\tau_n^{-1}\Delta x) + 1/(\tau_{m,11}^{-1}\Delta x_2)}. \quad (21)$$

Both τ_n^{-1} and $\tau_{m,ij}^{-1}$ are presumably Arrhenius-type processes and thus the rate at which each occurs can be theoretically modified by the application of σ_{ij} as given by TST [44]. However, since $\tau_{m,ij}^{-1}$ is a tensor property, a fourth-order tensor, $\Delta V_{kl}^{m,ij}$ must be used to describe the change in each component of $\tau_{m,ij}^{-1}$ with respect to σ_{kl} as given by

$$\Delta V_{kl}^{m,ij} = kT\frac{\partial \ln(\tau_{m,ij}^{-1})}{\partial \sigma_{kl}}. \quad (22)$$

Hence

$$\tau_{m,ij}^{-1} = \tau_{m,ij}(0)^{-1}\exp\left(\frac{\Delta V_{kl}^{m,ij}\sigma_{kl}}{kT}\right), \quad (23)$$

where $\tau_{m,ij}(0)^{-1}$ is the stress-free migration rate tensor. Similar models describe point defect motion in bulk Si [90]. Since $\tau_{m,12}(0)^{-1} = \tau_{m,21}(0)^{-1} = 0$ and the only term in σ_{ij} is σ_{11}, $\Delta V_{11}^{m,11}$ and $\Delta V_{11}^{m,22}$ are the only relevant terms in $\Delta V_{kl}^{m,ij}$. During ledge motion, the greatest in-plane volume change presumably occurs parallel to rather than orthogonal to a given migration direction which implies $|\Delta V_{11}^{m,22}| \ll |\Delta V_{11}^{m,11}|$. Furthermore, due to symmetry, $\Delta V_{11}^{m,11} = \Delta V_{22}^{m,22}$, $\Delta V_{11}^{m,22} = \Delta V_{22}^{m,11}$, and $\Delta V_{33}^{m,11} = \Delta V_{33}^{m,22}$. Thus, only migration along 1 is significantly altered by σ_{11}. Regarding τ_n^{-1}, a second order tensor, ΔV_{ij}^{n}, is used to describe the response of τ_n^{-1} with respect to σ_{ij} which is given by

$$\Delta V_{ij}^{n} = kT\frac{\partial \ln(\tau_n^{-1})}{\partial \sigma_{ij}}. \quad (24)$$

For the α-Si/(0 0 1)Si interface, (24) has the expanded form

$$\Delta V_{ij}^{n} = \begin{pmatrix} \Delta V_{11}^{n} & 0 & 0 \\ 0 & \Delta V_{11}^{n} & 0 \\ 0 & 0 & \Delta V_{33}^{n} \end{pmatrix}. \quad (25)$$

The nucleation of a crystal island causes volume change primarily in the growth direction rather than the in-plane directions, similar to the formation of a Si self-interstitial or vacancy near a surface [90]. Thus, $\Delta V_{11}^{n} \sim 0$ and only ΔV_{33}^{n} is relevant reducing (25) to approximately

$$\Delta V_{ij}^{n} = \begin{pmatrix} 0 & 0 & 0 \\ 0 & 0 & 0 \\ 0 & 0 & \Delta V_{33}^{n} \end{pmatrix} \quad (26)$$

and thus implying $\tau_n^{-1} \sim \tau_n^{-1}(0)$, where $\tau_n^{-1}(0)$ is the stress-free nucleation rate. Thus, (21) may be represented with the application of σ_{11} as

$$v = \frac{\Delta x}{\tau_n(0) + \tau_{m,11}(0)\exp(-\Delta V_{11}^{m,11}\sigma_{11}/kT)(\Delta x/\Delta x_1)} + \frac{\Delta x}{\tau_n(0) + \tau_{m,11}(0)(\Delta x/\Delta x_2)}. \quad (27)$$

In this case, $\Delta x_1 = \Delta x_2 = 0.38$ nm and (27) reduces further to

$$v = \frac{\Delta x}{\tau_n(0) + 2^{-3/2}\tau_{m,11}(0)\exp((-\Delta V_{11}^{m,11}\sigma_{11})/kT)} + \frac{\Delta x}{\tau_n(0) + 2^{-3/2}\tau_{m,11}(0)}. \quad (28)$$

Eq. (28) was fit to the data presented in Fig. 22 and $\tau_n(0)$, $\tau_{m,11}(0)$, and $\Delta V_{11}^{m,11}$ were calculated to be 29 ± 1 s, 0.36 ± 0.01 s, and $(12 \pm 1)\,\Omega$. The value of $\tau_n(0)$ is nearly two orders of magnitude greater than $\tau_{m,11}(0)$ which is consistent with prior observations suggesting that the nucleation rate is much slower than migration [43]. The positive value of $\Delta V_{11}^{m,11}$ suggests in-plane expansion associated with ledge migration. In the case of $\sigma_{11} \gg 0$, (28) reduces to the tensile saturation velocity

$$v_t \approx \frac{2\Delta x}{\tau_n(0)} \quad (29)$$

and the growth process is limited by the nucleation rate. However, in the case of $\sigma_{11} \ll 0$, (28) reduces to the compressive limit velocity

$$v_c \approx \frac{\Delta x}{\tau_n(0)} \quad (30)$$

and growth is still limited by nucleation with

$$\frac{v_t}{v_c} \approx 2. \quad (31)$$

Fig. 23 presents atomistic schematics of the SPEG migration process with different values of σ_{11}. In the case of $\sigma_{11} = 0$, shown in Fig. 23(a), a crystal island nucleates and the crystal ledges migrate (indicated by arrows) rapidly and evenly in both in-plane directions since $\tau_{m,ij}(0)^{-1}$ is isotropic. In the case of $\sigma_{11} > 0$, shown in Fig. 23(b), a crystal island nucleates and ledge migration along 1 is enhanced relative to 2. Hence, migration is rapid in both directions for cases of $\sigma_{11} \geq 0$. Thus, since the nucleation rate is unaltered by σ_{11} and much slower than the migration rates for $\sigma_{11} \geq 0$, the macroscopic growth rate is not significantly changed compared to the stress-free case. In the case of $\sigma_{11} < 0$, shown in Fig. 23(c), migration along 1 is retarded but unchanged along 2 thus implying $\tau_n < \tau_{m,11}$ and $\tau_{m,22} < \tau_n$. Therefore, the contribution to growth from ledge migration along 1 effectively becomes negligible compared to the contribution from ledge migration along 2. Thus, the macroscopic growth rate is effectively halved since migration along 2 is not altered. It is important to note the interfacial roughening in compression which generates off-axis growth fronts which grow up to ~25 times slower than [0 0 1]SPEG [19]. However, this cannot primarily account for the retardation with in-plane compression since $v_t/v_c \sim 2$.

The discrepancies between the presented data and the predictions and data of prior work are intriguing. The actual data from prior work does show enhancement (retardation) with in-plane tension (compression) in some (though not all) specimens. However, though (13) appears to describe the earlier work, there are many significant deviations in the data from this trend and, as a whole, the data is somewhat weakly-ordered. It is mentioned in ref. [52] that intra-sample thermal fluctuations may have confounded the results and the analysis techniques used were less site-specific relative those used in ref. [89]. Also, the range of σ_{11} in recent work was broader than that of earlier work. All of these issues may explain why the scatter in the prior data was larger than the recent data. However, even with these issues, Aziz et al. [52] were the first to observed and model the role of stress on SPEG.

Furthermore, the Aziz et al. model of stressed-SPEG assuming growth occurs via a single, unspecified atomistic process is a

Author's personal copy

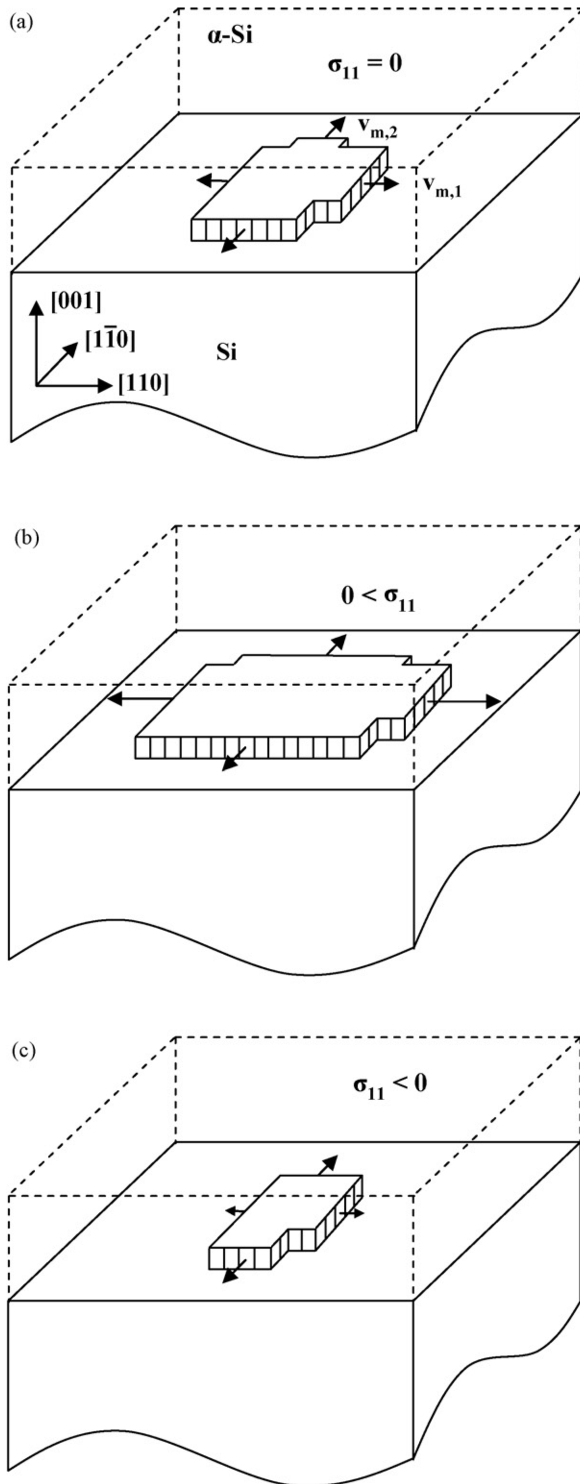

Fig. 23. Atomistic schematics of the in-plane SPEG process with (a) $\sigma_{11} = 0$, (b) $\sigma_{11} > 0$ and (c) $\sigma_{11} < 0$. Reproduced with permission from N.G. Rudawski, K.S. Jones, R. Gwilliam, Phys. Rev. Lett. in press (2008). Copyright (2008) by the American Physical Society

reasonable theory to explain the somewhat scattered results observed in ref. [52] due to the strong Arrhenius behavior of v in the absence of stress [11–13]. However, (28) provides an equally reasonable explanation for the prior data and the separation of nucleation and migration as discussed is critical for explaining the recent results.

Importantly, the recent results [89] provide greater understanding into the atomistic nature of the epitaxial solid–solid transformations of many materials systems. In particular, the large value of $\Delta V_{11}^{m,11}$ suggests that in-plane ledge motion is coordinated and involves the lateral advancement of multiple atoms along a growing island ledge rather than individual point defect motion as originally suggested [52]. Analogous coordination is observed in other systems such as deformation in metals which is typically characterized by activation volumes on the order of ~100 times the atomic volume of the material [91,92]. Thus, $\Delta V_{11}^{m,11} = (12 \pm 1)\Omega$ is reasonable considering migration may be coordinated and not due to independent defect motion.

It is provocative to predict the growth kinetics under biaxial in-plane stress using the recent model. In the case of biaxial tension, migration should be enhanced evenly in both in-plane directions and thus, the growth process should be nucleation limited. Thus, the growth kinetics should not be greatly different from the stress-free case. In fact, this was observed by Phen et al. [93]. Interestingly, this observation is in striking contrast to the predictions of Aziz et al. [52] where biaxial in-plane tension should cause growth rate enhancement. Regarding the case of in-plane biaxial compression, in this case both migration terms are retarded and thus nucleation is no longer limiting. Thus, the expression for v approaches something mathematically similar to (13). Therefore, in theory, the growth rate of Si with in-plane biaxial compression could be retarded beyond the compressive velocity limit observed for in-plane uniaxial stress to nearly zero. This is the same prediction as the Aziz et al. model [52]. It appears growth of biaxial compressively tressed SiGe follows this prediction [85–87], but the issues of Ge-influenced growth kinetics are a confounding variable [88].

4.3. Normal uniaxial compression

A prediction of the Aziz et al. [52] model is that the effect of normal uniaxial stress, σ_{33}, on SPEG kinetics would be characterized by

$$v = v(0)\exp\left(\frac{\Delta V_{33}^{*}\sigma_{33}}{kT}\right). \tag{32}$$

Since the predicted magnitude of ΔV_{33}^{*} is much larger than ΔV_{h}^{*}, though the sign is the same, it is predicted that normal compression should cause greater enhancement to the SPEG rate than hydrostatic pressure. Barvosa-Carter performed this experiment to test the prediction [73,94]. Fig. 24 presents a plot of the SPEG rate at 540 °C measured using TRR versus σ_{33} with the prediction from the Aziz et al. model [52]. There is qualitative agreement with the predicted behavior of (32) in that the growth

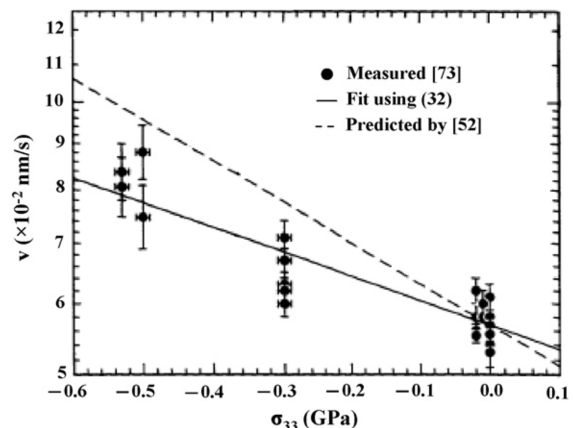

Fig. 24. Plot of SPEG rate vs. σ_{33} at 540 °C as measured using TRR [73]. Reproduced and modified with permission from W. Barvosa-Carter.

Author's personal copy

rate tends to show exponential enhancement with normal compression. However, the value of $\Delta V^*_{33} = (-0.35 \pm 0.04)\Omega$ is nearly half the predicted value of $-0.58\ \Omega$.

It is very interesting that the measured value of ΔV^*_{33} is very similar to $\Delta V^*_{\rm h} = (-0.28 \pm 0.03)\Omega$ measured by Lu et al. [77,78]. Thus, it appears that there may be no major difference in the SPEG kinetics under hydrostatic pressure or normal uniaxial stress. However, this implies that $\Delta V^*_{11} \sim 0$ which contradicts the original observations of Aziz et al. [52]. Thus, there appears to be some inconsistencies in the Aziz et al. model in explaining all the collected stress-dependent SPEG data. Interestingly, these observations are consistent with the model advanced by Rudawski et al. since nucleation is limiting in the absence of stress, and $\Delta V^{\rm n}_{11} \sim 0$ as advanced previously [89]. Thus, the exponential SPEG enhancement with hydrostatic pressure and normal uniaxial compression suggests $\Delta V^*_{33} = \Delta V^*_{\rm h} = \Delta V^{\rm n}_{33}$.

4.4. Morphological istability

An interesting result of growth with in-plane uniaxial compression is roughening of the α/crystalline interface. It was not known that this occurred in the early work by Aziz et al. since RBS was used for SPEG rate measurements [52]. However, later work showed that by forming a pre-rippled α/crystalline interface and effecting SPEG with in-plane compression caused the initial oscillations in the α/crystalline interface to amplify [84,95,96]. WBDF-XTEM micrographs of the as-implanted structure and the structure after annealing at 520 °C with in-plane compression are shown in Fig. 25(a) and (b). In the case of $\sigma_{11} \geq 0$, the perturbations are observed to dampen and the interface planarizes as shown in Fig. 25(c) [96].

In fact, this same instability occurs with an initially planar growth front. In recent work, partial growth at 525 °C in the absence of stress planarized the interface as shown in Fig. 26(a) [97]. With subsequent growth at 525 °C with in-plane compression, shown in Fig. 26(b), the resulting α/crystalline interface becomes unstable and starts to roughen. In the case of subsequent growth with in-plane tension, shown in Fig. 26(c), the resulting α/crystalline interface remains planar. This data suggests that there are small, sub-microscopic interface perturbations as the result of the growth process. This is elaborated on in a subsequent section.

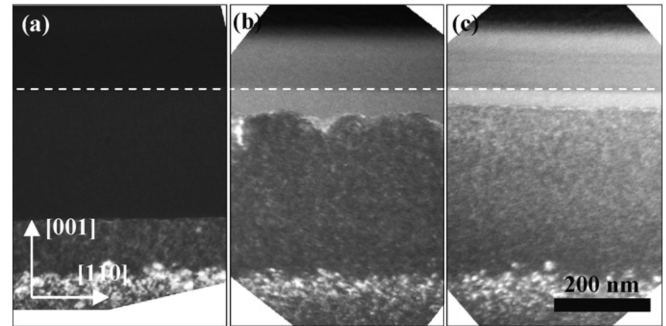

Fig. 26. (a) WBDF-XTEM image of a sample after annealing at 525 °C with $\sigma_{11} = 0$. WBDF-XTEM images of the specimen in (a) after additional annealing at 525 °C with different values of σ_{11}: (b) −1.3 GPa and (c) 1.3 GPa. Reproduced and modified with permission from N.G. Rudawski, K.S. Jones, R. Gwilliam, Appl. Phys. Lett. 91 (17) (2007) 172103. Copyright (2007) by the American Institute of Physics.

Both the Aziz et al. [52] model and the Rudawski et al. [89] model derived from recent experiments predict this instability. In the case of a growing front with perturbations under in-plane macroscopic compression, shown in Fig. 27(a), there is localized concentrated in-plane compressive stress ($\sigma^{\rm local}_{11}$) in the troughs of the front and localized tensile stress in the peaks of the front, since the amorphous phase is near fully relaxed at $T \sim 500$ °C [66,67]. Thus, as per (13) and (28), the peaks grow faster than the troughs and the growth front roughens. On the other hand, the application of macroscopic tension, shown in Fig. 27(b), causes a reversal of the localized stress states which leads to eventual dampening of any perturbations in the growth front due to kinetic limitations. Thus, both the prior and new models provide explanations for the observed morphological instability. This instability is also observed in growth of the in-plane compressively trained SiGe system [98].

However, even though both models correctly predict the instability, the Rudawski et al. model [89] predicts weaker sensitivity of the resulting $R_{\rm RMS}$ (due to the limits of v with in-plane tension and compression) while the Aziz et al. model [52] predicts increasing roughness with increasing in-plane tension. In fact, $R_{\rm RMS}$ is not observed to show much variation with in-plane stress as the values are similar for $-1.3 \leq \sigma_{11} \leq -0.5$ GPa, as shown in Fig. 20(b)–(d) which is consistent with the Rudawski et al. model. This also corroborates the Rudawski et al. model for stress-dependent SPEG which suggested no effect of in-plane tension on v.

4.5. Shortcomings of stress-dependent SPEG models

Two models have thus far been advanced to explain different and somewhat contradictory sets of stress-dependent SPEG data.

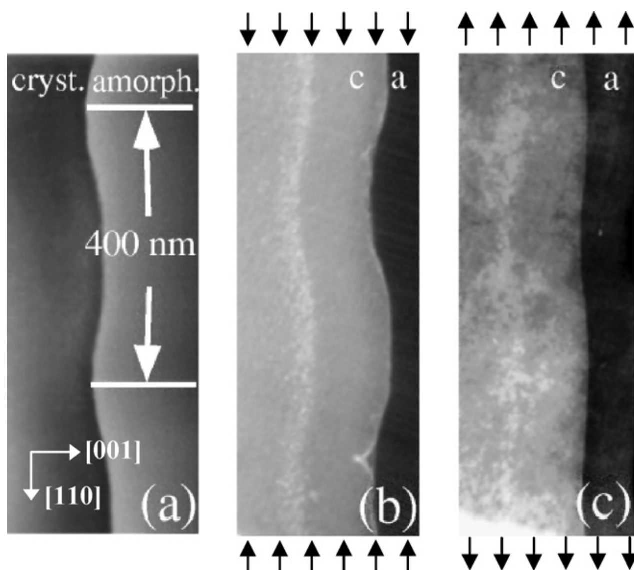

Fig. 25. (a) WBDF-XTEM image of an as-implanted specimen with a pre-rippled α/crystalline interface. WBDF-XTEM images of the specimen in (a) after annealing at 520 °C with (b) $\sigma_{11} < 0$ and (c) $\sigma_{11} \geq 0$ [96]. Reproduced and modified with permission from J.F. Sage, W. Barvosa-Carter, M.J. Aziz, Appl. Phys. Lett. 77 (4) (2000) 516. Copyright (2000) by the American Institute of Physics.

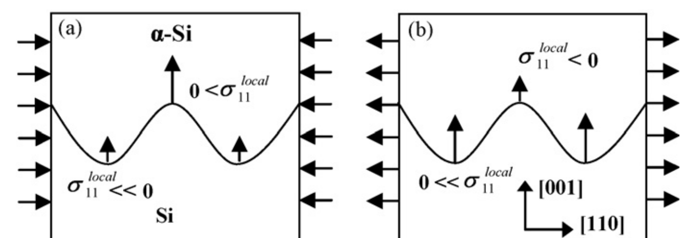

Fig. 27. Schematics of α/crystalline interface morphological stability with macroscopic in-plane (a) compression and (b) tension. Reproduced with permission from N.G. Rudawski, K.S. Jones, R. Gwilliam, Phys. Rev. Lett. in press (2008). Copyright (2008) by the American Physical Society.

Author's personal copy

However, it is important to note that the issues with interfacial roughening force both models to make some notable assumptions and simplifications. Foremost, the anisotropy of the SPEG rate presented in Fig. 5 is at least partially responsible for some, though not all, of the observed retardations with in-plane compression. Furthermore, when the growing α/crystalline interface becomes excessively rough, it is difficult to characterize the exact amount of growth which has occurred even though the method outlined in Section 3.3.2 attempts to account for this. In both cases, the models have been used to extract and advance different activation volume terms for (0 0 1)SPEG, but it is unknown if these activation volumes are orientation dependent. The localized stress states at an interface with perturbations are also very complicated due to variations in curvature. Thus, it is nearly impossible to accurately account for all these variables when modeling stress-dependent SPEG though there have been some notable attempts [99,100]. The models would be more accurate if the growth front remained planar for all stress states but this is not the case. However, even with the shortcomings of each model, both models correctly predict the roughening of an initially planar α/crystalline interface with in-plane compression.

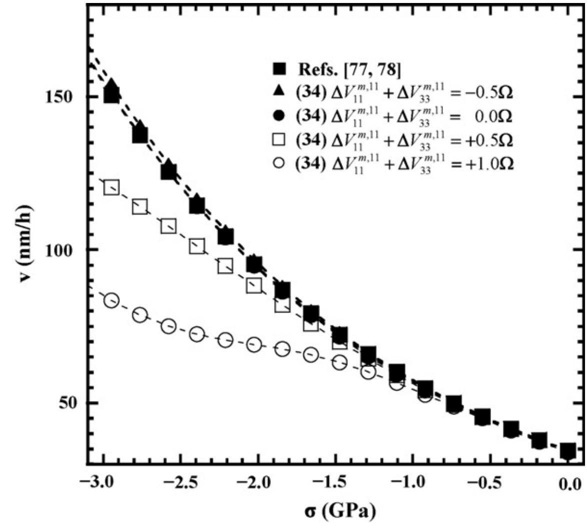

Fig. 28. Predicted SPEG vs. σ behavior at 525 °C using different models.

4.6. Unification of earlier and recent stressed-SPEG results

As evidenced by the first experiments studying hydrostatic pressure on SPEG kinetics, the data is quite compelling that hydrostatic pressure does indeed cause exponential enhancement to the growth rates. Likewise, the recent work by Rudawski et al. of uniaxial stress effects on SPEG produced similarly striking and compelling data. Thus, it remains to be seen if both sets of data are consistent within the SPEG model recently advanced by Rudawski et al. [89].

In the most general case of σ_{ij}, v is given by

$$v=\frac{\Delta x}{\tau_n(0)\exp(-\Delta V_{33}^{n}\sigma_{33}/kT)+2^{-3/2}\tau_{m,11}(0)\exp(-(\Delta V_{11}^{m,11}\sigma_{11}+\Delta V_{33}^{m,11}\sigma_{33})/kT)}+\frac{\Delta x}{\tau_n(0)\exp(-\Delta V_{33}^{n}\sigma_{33}/kT)+2^{-3/2}\tau_{m,11}(0)\exp(-(\Delta V_{11}^{m,11}\sigma_{22}+\Delta V_{33}^{m,11}\sigma_{33})/kT)}. \quad (33)$$

In the case of hydrostatic pressure, (33) reduces to

$$v=\frac{2\Delta x}{\tau_n(0)\exp(-\Delta V_{33}^{n}\sigma/kT)+2^{-3/2}\tau_{m,11}(0)\exp(-(\Delta V_{11}^{m,11}+\Delta V_{33}^{m,11})\sigma/kT)} \quad (34)$$

since $\sigma_{11}=\sigma_{22}=\sigma_{33}=\sigma$. Using the results of hydrostatic pressure-enhanced SPEG, ΔV_{33}^{n} is taken to be $(0.28\pm0.03)\,\Omega$ [77,78]. From the recent in-plane uniaxial stress experiments, $\Delta V_{11}^{m,11}=(12\pm1)\Omega$. Thus, $\Delta V_{33}^{m,11}$ is the only remaining free parameter in (34).

Fig. 28 presents the predicted SPEG behavior in hydrostatic stress as predicted by Lu et al. at T = 525 °C using the stress-free growth velocity of 34 ± 2 nm/h presented in Fig. 22 [77,78]. The predicted behavior of (34) at T = 525 °C fit using $\tau_n(0)$ = 29 s and $\tau_{m,11}(0)$ = 0.36 s as calculated in recent uniaxial stress experiments with different values of $\Delta V_{11}^{m,11}+\Delta V_{33}^{m,11}$ provided as well. In the case of $\Delta V_{11}^{m,11}+\Delta V_{33}^{m,11}>0$, both models match well for lower values of stress, but (33) predicts lower SPEG rates at higher stresses than predicted by Lu et al. [78]. In contrast, when $\Delta V_{11}^{m,11}+\Delta V_{33}^{m,11}\leq 0$, the two models match quite well for all values of pressure. Thus, there may be a net volumetric compression associated with the migration transition state. This is consistent with the observation that α-Si is less dense than the crystalline counterpart [81]. Thus, $\Delta V_{33}^{m,11}$ must be on the order of −12 Ω which is very large, similarly to the in-plane term, but this value may once again be reasonable considering the likelihood of coordinated migration proposed for the uniaxial stress data. Thus, since nucleation is slower than migration, (34) is approximately

$$v\approx\frac{2\Delta x}{\tau_n(0)}\exp\left(\frac{\Delta V_{33}^{n}\sigma}{kT}\right), \quad (35)$$

which is the equivalent mathematical expression given in (12).

This also explains the similar results of SPEG under uniaxial normal compression measured by Barvosa-Carter compared to SPEG measured under hydrostatic pressure [73]. Since all terms except ΔV_{33}^{n} are zero in ΔV_{ij}^{n}, the introduction of in-plane stresses does not change the nucleation rate. Regarding migration, normal uniaxial compression should cause greater migration rate enhancements than pressure since $|\Delta V_{33}^{m,11}|>|\Delta V_{11}^{m,11}+\Delta V_{33}^{m,11}|$. However, since migration is still much faster in these cases of stress, the process is still nucleation limited.

4.7. A new atomistic picture of SPEG

While it is important that the newly advanced model of stress-dependent SPEG correctly accounts for all phenomena observed in stressed SPEG, it remains to be seen if the model can be extended to address the phenomena observed in stress-free SPEG. Since the model is based on the defect-mediation model, impurity and substrate orientation effects outlined early are accounted for and are not addressed further. However, the greatest question of Si SPEG centers on the meaning of the observed ΔG^* = 2.7 eV which to date has never been answered.

One of the benefits of applying in-plane stress is that a single-growth process (migration) can be altered thus allowing greater examination of the other process (nucleation). This leads to extraction of the different nucleation and migration times at a given temperature. Thus, repeating the experiment of uniaxially stressed SPEG at other temperatures allows this.

Table 1
Nucleation and migration parameters

T (°C)	$\tau_n(0)$ (s)	$\tau_{m,11}(0)$ (s)	$\Delta V_{11}^{m,11}$ (Ω)
500	4.08	1.44 ± 0.10	12 ± 1
525	1.02	0.36 ± 0.03	12 ± 1
550	0.28	0.10 ± 0.01	12 ± 1
575	0.11	0.04 ± 0.01	12 ± 1

Author's personal copy

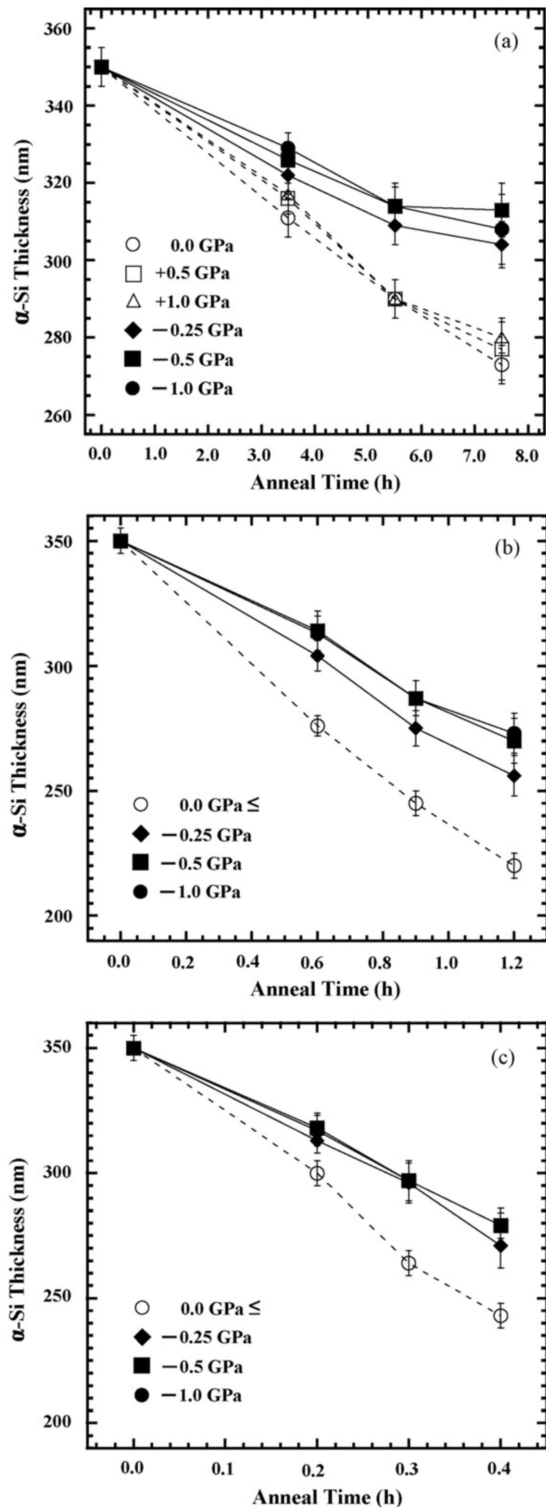

Fig. 29. Plots of α-Si thickness vs. annealing time for different σ_{11} as measured using WBDF-XTEM at different values of T: (a) 500 °C, (b) 550 °C, and (c) 575 °C.

Fig. 29(a)–(c) present plots of α-Si thickness versus time for $T = 500$–575 °C for $-1.0\ \text{GPa} \leq \sigma_{11} \leq 1.0\ \text{GPa}$ as measured using WBDF-XTEM. In cases of $\sigma_{11} \geq 0$, no significant differences in growth versus time behavior were observed at any temperature. In the compressive cases, the amounts of growth were much less and appeared to reach limiting amounts. Thus, this data is very consistent with the data collected at 525 °C.

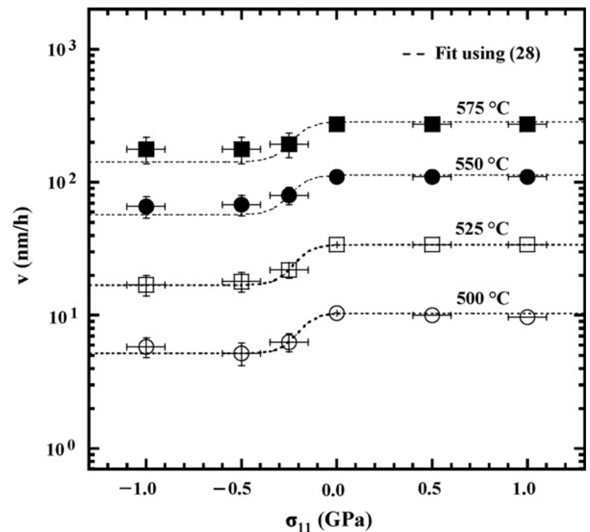

Fig. 30. Plot of v vs. σ_{11} for different T as measured using WBDF-XTEM.

Fig. 30 presents a plot of v versus σ_{11} for $T = 500$–575 °C as calculated from Fig. 29. Each value of T displays similar dependence of v on σ_{11}. For cases of $\sigma_{11} \geq 0$, v does not measurably change and for cases of $\sigma_{11} \leq -0.5$ GPa, v is retarded to a limiting value. A very sharp transition between the limiting velocity in compression and the saturation in tension occurs for $-0.5\ \text{GPa} < \sigma_{11} < 0\ \text{GPa}$ in all cases, indicative of significant in-plane expansion associated with mediating-defect migration. Using (28), $\tau_{\text{n}}(0)$, $\tau_{\text{m},11}(0)$, and $\Delta V_{11}^{\text{m},11}$ were calculated for each T as presented in Table 1. For each temperature, the nucleation time is nearly two orders of magnitude greater than the migration time which is consistent with prior observations with all values decreasing with increasing temperature [43]. The value of $\Delta V_{11}^{\text{m},11}$ shows no detectable variation with temperature indicating the coordinated defect migration characterized by $\Delta V_{11}^{\text{m},11} = (12 \pm 1)\Omega$ observed at 525 °C still exists in this temperature range. For $T = 550$ and 575 °C, there are significant positive deviations from predictions with in-plane compression. However, the error in compressive SPEG rates at higher temperatures is much larger due to the interfacial roughening and the faster growth rates and the model is still within experimental error.

It is likely that the nucleation and migration parameters obey the relationship given by

$$\tau_i(0)^{-1} = \tau_{i0}^{-1} \exp\left(\frac{-\Delta G_i^*}{kT}\right), \tag{36}$$

where τ_{i0}^{-1} is a temperature-independent pre-exponential factor, $\tau_i(0)^{-1}$ the rate for process i to occur without stress, and ΔG_i^* is the activation barrier for the process [44]. The logarithm of $\tau_{\text{n}}(0)^{-1}$ and $\tau_{\text{m},11}(0)^{-1}$ are plotted versus the reciprocal of kT as presented in Fig. 31. The plots appear linear in each case suggesting (35) is a very decent fit for each parameter. Thus, ΔG_{n}^*, and $\Delta G_{\text{m},11}^*$ are calculated to be 2.5 ± 0.1 and 2.7 ± 0.1 eV with $\tau_{\text{n}0}$ and $\tau_{\text{m},110}$ calculated to be and $(4.8 \pm 0.1) \times 10^{-16}$ and $(2.5 \pm 0.1) \times 10^{-18}$ s, respectively.[1] The similarity in the activation energies is interesting, since it was postulated that migration had a lower activation barrier than nucleation. The Si–Si bond energy is ∼2.5 eV, for reference [101]. Physically, it is somewhat intuitive to rationalize that the activation barriers should be similar for both processes and similar to the Si–Si bond energy since on the most basic level, SPEG is the rearrangement, breaking, and reforming of Si–Si bonds. Thus, at the most basic

[1] The activation energy for migration is not a tensor property but may be orientation dependent.

Author's personal copy

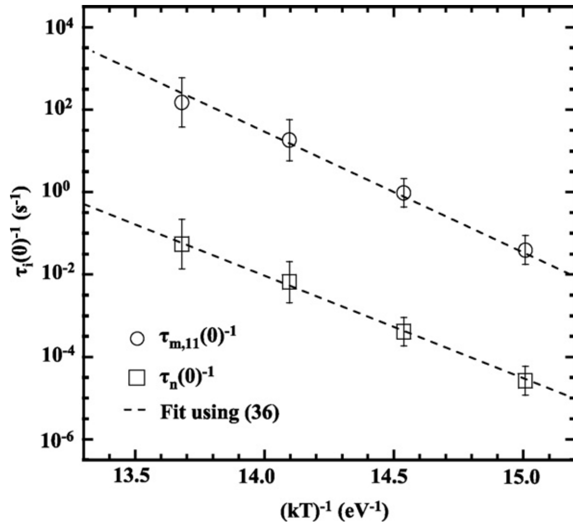

Fig. 31. Plot of stress-free nucleation and migration parameters vs. the reciprocal of *kT*.

atomistic level, nucleation and migration processes may be the same process of Si–Si bond rearrangement. This also explains the observation of the activation energy of the SPEG velocity being independent of substrate orientation since bond-rearrangement energetics are presumably not orientation dependent [19]. Therefore, it appears the pre-exponential factors are almost entirely responsible for the differences between migration and nucleation rates. The difference between the two factors may be related to the relative scales or geometry of the two processes. In the case of nucleation, presumably only small groups of atoms must rearrange to form a crystal island to start growth while in the case of migration large numbers of atoms along the island ledges are involved in continuing growth (coordinated motion).

It is interesting to compare these results with the study of Williams et al. which showed that ΔG^* for SPEG enacted via ion irradiation was nearly an order of magnitude smaller than ΔG^* for SPEG enacted via furnace annealing since it was speculated that the activation barrier for nucleation was reduced in the former case [35]. However, if the activation barrier for migration was unaffected, migration would then be the limiting step during SPEG and the value of ΔG^* should still be close to $\sim$2.7 eV. The fact that this was not the case indicates that ion bombardment influenced both nucleation and migration processes to the same degree and this is a reasonable conclusion to draw since nucleation and migration processes both involve the same basic rearrangement of Si–Si bonds.

Thus, the nucleation term dominates (21) due to the magnitude of τ_{n0} and in the absence of any stress and can be reduced to

$$v \approx \frac{2\Delta x}{\tau_{n0}} \exp\left(\frac{-\Delta G_n^*}{kT}\right). \quad (37)$$

Thus, $v_0 = 2\Delta x/\tau_{n0}$ is the pre-exponential factor in (2) with $v_0 = (5.8 \pm 0.5) \times 10^7$ cm/s within the range of values for v_0 calculated in prior work [12,13,19]. The slightly lower value of ΔG_n^* compared to the accepted value of ΔG^* = 2.7 eV may be related to the larger relative portion of ramp-up time to total anneal time in higher temperature samples as well as the larger error in SPEG rates observed with in-plane tension at higher temperatures. Therefore, the observed activation energy for SPEG of α-Si created via ion-implantation is indicative of the rate-limiting step of defect nucleation.

The results provide a greater understanding of the role of individual atomistic processes on the value of ΔG^* for the epitaxial α-Si/Si transformation. Important is the observation that the activation barriers for migration and nucleation processes are nearly equivalent and similar to the Si–Si bond energy. It has long been known that nucleation was slower than migration but it was not understood that the difference in the rates was not due to energetic considerations but may possibly be due to the relative scale of nucleation compared to migration. However, it can now be advanced that ΔG^* observed for SPEG of α-Si is reflective of the activation energy for mediating defect nucleation and the scale of nucleation.

Importantly, while the migration process can be assumed two-dimensional in nature, the same cannot necessarily be said of nucleation. Furthermore, while the mathematical construct presented in (28) can correctly predict α/crystalline interfacial roughening with $\sigma_{11} < 0$, as shown in Fig. 27, it is interesting to consider if the issue of non-planar nucleation (before layer completion) may be an influence or an explanation in morphological stability. It may simply be the case that a perturbation of a few monolayers of Si is large enough to shift the localized stress state to facilitate roughening since in theory the smallest perturbation may shift the stress state and as was previously shown, the magnitude of in-plane compression need not be very high to achieve significant retardation.

Additionally, it is difficult to study the nature of the nucleation and migration processes since it is not possible to observe the growth in plan-view. If plan-view study of SPEG via atomic force or scanning tunneling electron microscopy were possible, much could be ascertained regarding the morphology of the growing islands and the nature of nucleation. Thus, it remains unknown if nucleation possesses a non-planar component in addition to the advanced planar component.

By way of comparison with homoepitaxial growth from the vapor phase, the phenomenon of a critical radius (R_c) necessary for nucleation is well established [102]. The theory states that a two-dimensional crystal island growing in the plane of the vapor/solid interface must achieve a radius beyond R_c to start nucleating a second crystal island on top of itself. Furthermore, this theory is very successful at explaining morphological instabilities associated with the vapor-phase homoepitaxial growth of many semiconductor systems [103–106]. However, the case of SPEG of α-Si is inherently different from vapor-phase epitaxy since the atoms used for growth in the former case are presumably not required to diffuse any significant distance along the growth front. Furthermore, the R_c theory predicts complicated temperature-sensitive interface instability via a complex interplay of nucleation and surface diffusion processes. In contrast, SPEG of Si is always planar (in the absence of any applied stress) for all growth temperatures. Therefore, R_c may not be relevant in considerations of Si SPEG, but at present this is unclear.

Another perspective for considering roughening during SPEG with $\sigma_{11} < 0$ may be that of a growth mode transition which is associated with vapor-phase heteroepitaxy. Depending on the strain and interface energy between the substrate and epitaxial film, the film may grow by layer-by-layer (Frank–van der Merwe), island growth (Volmer–Weber), and layer-by-layer plus islands growth (Stranski–Krastanow) modes [107–109]. Typically, the interface energy is very small for semiconductor heteroepitaxy and strain energy controls the film morphology during growth. Hence, it may be reasonable to consider that the application of $\sigma_{11} < 0$ changes the growth mode from Frank–van der Merwe to Volmer–Weber or Stranski–Krastanow growth modes thus suggesting morphological instability during stressed SPEG of Si is strain driven as reported by others studying vapor-phase heteroepitaxy [110,111]. However, fundamental differences between vapor-phase heteroepitaxy and solid-phase homoepitaxy suggest otherwise. During the initial stages of vapor-phase heteroepitaxy, the

Author's personal copy

strain is concentrated in the film while for stressed SPEG of Si the strain is uniform throughout the substrate and film. Thus, there is effectively no strain energy consideration between the film and substrate for stressed SPEG of Si and morphological instabilities in such cases cannot be strain driven. Therefore, it appears interfacial roughening during stressed SPEG is entirely kinetically driven.

5. Conclusions

In this review, the kinetics of SPEG of α-Si created via ion-implantation under applied stress was examined. The earliest experiments of stressed SPEG revealed exponential enhancement to the growth velocity with hydrostatic pressure. Subsequent experiments studying the effect of in-plane stress on SPEG kinetics produced different results among researchers. The initial data suggested enhancement to the α/crystalline interface velocity with in-plane tension and retardation in compression. Thus, in conjunction with the data from hydrostatic stress results, it was advanced by Aziz et al. that stress-dependent SPEG could be modeled assuming a single-atomistic process using the activation strain tensor. This was in contrast to the defect-mediated growth model advanced by others which suggested the idea of nucleation and migration processes influencing kinetics.

Later experiments confirmed retardation with in-plane compression but did not reveal any rate enhancement with in-plane tension. Furthermore, the velocity was observed to reach a limit in compression. Thus, a counter-model was advanced by Rudawski et al. which proposed that nucleation and migration processes suffer different stress dependencies. The model was based on the defect-mediated SPEG model presented to explain different phenomena in stress-free SPEG. Results also indicated the migration process is coordinated in nature, as evidenced by the large activation volume for in-plane migration. The counter-model also predicts the exponentially enhanced growth rates observed with hydrostatic pressure by assuming the migration transition state involves a net volumetric contraction.

Morphological instability of the growth fronts, observed with in-plane compression, is an interesting and important consideration in stressed SPEG. Both the initial and recent models of stressed SPEG can account for this model. However, the initial model predicts greater stress dependence of the resulting α/crystalline interface roughness than observed using XTEM. The recent model does, however, account for the relative insensitivity of the interfacial roughness with stress. Interfacial roughening also complicates modeling the growth process due to the formation of off-axis growth front and likely anisotropy of the transition states. Thus, it is important to understand that the stressed SPEG process is more complex than different researchers have modeled it.

Stressed SPEG also provided a window into examining the different atomistic processes associated with growth. By selectively altering a single-atomistic process, it was possible to characterize the energetics of nucleation and migration processes. The results suggested that SPEG is composed of nucleation and migration processes with nucleation likely being responsible for the observed activation energy of 2.7 eV for stress-free SPEG. This builds upon the defect-mediation model of SPEG, but also accounts for the recent stress-related results from Rudawski et al.

Acknowledgements

The authors acknowledge the Semiconductor Research Corporation for funding this research. The Major Analytical Instrumentation Center at the University of Florida is acknowledged for use of the focused ion beam and transmission electron microscopy facilities.

References

[1] J.W. Mayer, L. Eriksson, J.A. Davies, Can. J. Phys. 45 (1968) 663.
[2] J.A. Roth, C.L. Anderson, Appl. Phys. Lett. 31 (10) (1977) 689.
[3] P.R. Chidambaram, C. Bowen, S. Chakravarthi, C. Machala, R. Wise, IEEE Trans. Electron. Dev. 53 (5) (2006) 944.
[4] S.M. Hu, Appl. Phys. Lett. 32 (1) (1978) 5.
[5] S.M. Hu, J. Appl. Phys. 50 (7) (1979) 4661.
[6] S.M. Hu, J. Appl. Phys. 70 (6) (1991) R53.
[7] G.-Q. Lu, E. Nygren, M.J. Aziz, D. Turnbull, C.W. White, Appl. Phys. Lett. 56 (2) (1990) 137.
[8] P.H. Leo, W.W. Mullins, R.F. Sekerka, J. Viñals, Acta Metall. Mater 38 (8) (1990) 1573.
[9] E. Chason, M.J. Aziz, J. Non-Cryst. Solids 130 (2) (1991) 204.
[10] V.J. Fratello, J.F. Hays, D. Turnbull, J. Appl. Phys. 51 (9) (1980) 4718.
[11] J.A. Roth, G.L. Olson, D.C. Jacobson, J.M. Poate, Appl. Phys. Lett. 57 (13) (1990) 1340.
[12] J.M. Poate, S. Coffa, D.C. Jacobson, A. Polman, J.A. Roth, G.L. Olson, S. Roorda, W. Sinke, J.S. Custer, M.O. Thompson, F. Spaepen, E. Donovan, Nucl. Inst. Meth. Phys. Res. B B55 (1991) 533.
[13] G.L. Olsen, J.A. Roth, Mater. Sci. Rep. 3 (1988) 1.
[14] W.O. Adekoya, M. Hage-Ali, J.C. Muller, P. Siffert, J. Appl. Phys. 64 (2) (1988) 666.
[15] L. Csepregi, E.F. Kennedy, T.J. Gallagher, J.W. Mayer, T.W. Sigmon, J. Appl. Phys. 48 (10) (1977) 4234.
[16] J.S. Williams, R.G. Elliman, Phys. Rev. Lett. 51 (12) (1983) 1069.
[17] B.C. Johnson, J.C. McCallum, Phys. Rev. B 76 (4) (2007) 045206.
[18] E.F. Kennedy, L. Csepregi, J.W. Mayer, T.W. Sigmon, J. Appl. Phys. 48 (1997) 4241.
[19] L. Csepregi, E.F. Kennedy, T.W. Sigmon, J. Appl. Phys. 49 (7) (1978) 3906.
[20] N.G. Rudawski, K.N. Siebein, K.S. Jones, Appl. Phys. Lett. 89 (8) (2006) 082107.
[21] N.G. Rudawski, K.S. Jones, R.G. Elliman, J. Vac. Sci. Technol. B 26 (1) (2007) 435.
[22] C. Ross, K.S. Jones, Mater. Res. Soc. Symp. Proc. 810 (2004) C10.4.
[23] K.L. Saenger, J.P. de Souza, K.E. Fogel, J.A. Ott, A. Reznicek, C.Y. Sung, D.K. Sadana, H. Yin, Appl. Phys. Lett. 87 (2005) 221911.
[24] K.L. Saenger, J.P. de Souza, K.E. Fogel, J.A. Ott, C.Y. Sung, D.K. Sadana, H. Yin, J. Appl. Phys. 101 (2006) 024908.
[25] Y.G. Shin, J.Y. Lee, M.H. Park, H.K. Kang, J. Cryst. Growth 233 (4) (2001) 673.
[26] Y.G. Shin, J.Y. Lee, M.H. Park, H.K. Kang, J. Cryst. Growth 231 (1–2) (2001) 107.
[27] Y.G. Shin, J.Y. Lee, M.H. Park, H.K. Kang, Jpn. J. Appl. Phys. 40 (11) (2001) 6192.
[28] M. Yang, V.W.C. Chan, K.K. Chan, L. Shi, D.M. Fried, J.H. Stathis, A.I. Chou, E. Gusev, J.A. Ott, L.E. Burns, M.V. Fischetti, M. Ieong, IEEE Trans. Electron Dev. 53 (5) (2005) 965.
[29] T. Sato, Y. Takeishi, H. Hara, Jpn. J. Appl. Phys. 8 (5) (1969) 588.
[30] D. Colman, R.T. Bate, J.P. Mize, J. Appl. Phys. 39 (4) (1968) 1923.
[31] H. Cerva, K.-H. Kusters, J. Appl. Phys. 66 (10) (1989) 4723.
[32] H. Cerva, W. Bergholz, J. Electrochem. Soc. 140 (3) (1993) 780.
[33] H. Cerva, Defect Diffus. Forum 148 (1997) 103.
[34] A. Bousetta, J.A. Vandenberg, R. Valizadeh, D.G. Armour, P.C. Zalm, Nucl. Inst. Meth. Phys. Res. B 55 (1–4) (1991) 565.
[35] J. Vonborany, R. Kogler, Nucl. Inst. Meth. Phys. Res. A 326 (1–2) (1993) 42.
[36] J. Narayan, J. Appl. Phys. 53 (12) (1982) 8607.
[37] J.M. Poate, J.S. Williams, Ion Implantation and Beam Processing, Academic Press, New York, 1984, pp. 13–57.
[38] F. Spaepen, Acta Metall. 26 (1978) 1167.
[39] J. Narayan, O.W. Holland, Phys. Status Solidi A 73 (1982) 225.
[40] J. Washburn, C.S. Murty, D.K. Sadana, P. Byrne, R. Gronsky, N. Cheung, R. Kilass, Nucl. Inst. Meth. 209 (1983) 345.
[41] H. Muller, W.K. Chu, J. Gyulai, J.W. Mayer, T.W. Sigmon, T.R. Cass, Appl. Phys. Lett. 26 (1975) 293.
[42] M.D. Rechtin, P.P. Pronko, G. Foti, L. Csepregi, E.F. Kennedy, J.W. Mayer, Philos. Mag. A 37 (1978) 605.
[43] J.S. Williams, R.G. Elliman, W.L. Brown, T.E. Seidel, Phys. Rev. Lett. 55 (14) (1985) 1482.
[44] S. Glasstone, K.J. Laidler, H. Eyring, The Theory of Rate Processes, McGraw-Hill, New York, 1948.
[45] E.P. Donovan, F. Spaepen, D. Turnbull, J.M. Poate, D.C. Jacobson, Appl. Phys. Lett. 42 (1983) 698.
[46] E.P. Donovan, F. Spaepen, D. Turnbull, J.M. Poate, D.C. Jacobson, J. Appl. Phys. 57 (1985) 1795.
[47] A.K. Sheridan, J. Anwar, Chem. Mater. 8 (1996) 1042.
[48] K.E. Rajab, R.D. Doherty, Acta Metall. 37 (10) (1989) 2709.
[49] J.M. Howe, H.I. Aaronson, R. Gronsky, Acta Metall. 33 (4) (1985) 639.
[50] P. Kringhoj, R.G. Elliman, Phys. Rev. Lett. 73 (6) (1994) 858.
[51] P.M. Fahey, P.B. Griffin, J.D. Plummer, Rev. Mod. Phys. 61 (2) (1989) 289.
[52] M.J. Aziz, P.C. Sabin, G.-Q. Lu, Phys. Rev. B 44 (18) (1991) 9812.
[53] J.F. Ziegler, Nucl. Inst. Meth. Phys. Res. B 219–220 (2003) 1027.
[54] K.S. Jones, S. Prussin, E.R. Weber, Appl. Phys. A 45 (1) (1988) 1.
[55] G.J. Piermarini, S. Block, J.D. Barnett, R.A. Forman, J. Appl. Phys. 46 (1975) 2774.
[56] A. Jayaraman, Rev. Sci. Instrum. 57 (1986) 1013.
[57] F.R. Boyd, J.R. England, J. Geophys. Res. 65 (1960) 741.
[58] J.J. Wortman, R.A. Evans, J. Appl. Phys. 36 (1) (1965) 153.
[59] C.R. Olson, E. Kuryliw, B.E. Jones, K.S. Jones, J. Vac. Sci. Technol. B 24 (1) (2006) 446.
[60] S.P. Nikanorov, Yu.A. Burenkov, A.V. Stepanov, Sov. Phys. Solid State 13 (10) (1971) 2516.
[61] M. Brede, K.J. Hsia, A.S. Argon, J. Appl. Phys. 70 (2) (1991) 758.

Author's personal copy

[62] K. Yasutake, J. Murakami, M. Umeno, H. Kawabe, Jpn. J. Appl. Phys. 21 (5) (1982) L288.
[63] D.S. Walters, S.M. Spearing, Scripta Mater. 42 (2000) 769.
[64] T. Fukuda, M. Koizuka, J. Appl. Phys. 74 (4) (1993) 2420.
[65] T.S. Gross, V.K. Mathews, R.J. De Angelis, K. Okazaki, Mater. Sci. Eng A 117 (1989) 75.
[66] C.A. Volkert, J. Appl. Phys. 70 (7) (1991) 3521.
[67] S.I. Tan, B.S. Berry, B.L. Crowder, Appl. Phys. Lett. 20 (2) (1972) 88.
[68] T. Ando, S. Li, S. Nakao, T. Kasai, H. Tanaka, M. Shikida, K. Sato, Fatigue Fract. Eng. Mater. Struct. 28 (8) (2005) 687.
[69] F. Ebrahimi, L. Kalwani, Mater. Sci. Eng. A 268 (1999) 116.
[70] X.P. Li, T. Kasai, S. Nakao, H. Tanaka, T. Ando, M. Shikida, K. Sato, Sens. Actuat. A 119 (1) (2005) 229.
[71] M. Tanaka, K. Higashida, H. Nakashima, H. Takagi, M. Fujiwara, Mater. Trans. 44 (4) (2003) 681.
[72] M. Tanaka, K. Higashida, H. Nakashima, H. Takagi, M. Fujiwara, J. Jpn. Inst. Met. 68 (9) (2004) 787.
[73] W. Barvosa-Carter, PhD Thesis, 1997.
[74] L. Csepregi, J.W. Mayer, T.W. Sigmon, Phys. Lett. A 54 (1975) 157.
[75] L. Csepregi, J.W. Mayer, T.W. Sigmon, Appl. Phys. Lett. 29 (1976) 92.
[76] E. Nygren, M.J. Aziz, D. Turnbull, Appl. Phys. Lett. 47 (3) (1985) 232.
[77] G.-Q. Lu, E. Nygren, M.J. Aziz, D. Turnbull, C.W. White, Appl. Phys. Lett. 54 (1989) 2583.
[78] G.-Q. Lu, E. Nygren, M.J. Aziz, J. Appl. Phys. 70 (10) (1991) 5323.
[79] T.K. Chaki, Philos. Mag. Lett. 63 (6) (1991) 303.
[80] T.K. Chaki, Phys. Status Solidi A 142 (1) (1994) 153.
[81] J.S. Custer, M.O. Thompson, D.C. Jacobson, J.M. Poate, S. Roorda, W.C. Sinke, F. Spaepen, Appl. Phys. Lett. 64 (4) (1994) 437.
[82] W. Barvosa-Carter, M.J. Aziz, Appl. Phys. Lett. 79 (3) (2001) 356.
[83] W. Barvosa-Carter, M.J. Aziz, Mater. Res. Soc. Symp. Proc. 356 (1995) 87.
[84] W. Barvosa-Carter, M.J. Aziz, A.-V. Phan, T. Kaplan, L.J. Gray, J. Appl. Phys. 96 (10) (2004) 5462.
[85] Q.-Z. Hong, J.G. Zhu, J.W. Mayer, W. Xia, S.S. Lau, J. Appl. Phys. 71 (4) (1992) 1768.
[86] F. Corni, S. Frabboni, R. Tonini, G. Ottaviani, G. Queirolo, J. Appl. Phys. 79 (7) (1996) 3528.
[87] C. Lee, T.E. Haynes, K.S. Jones, Appl. Phys. Lett. 62 (5) (1993) 501.
[88] T.E. Haynes, M.J. Antonell, C.A. Lee, K.S. Jones, Phys. Rev. B 51 (12) (1995) 7762.
[89] N.G. Rudawski, K.S. Jones, R. Gwilliam, Phys. Rev. Lett. (2008), in press.
[90] M.J. Aziz, Appl. Phys. Lett. 70 (21) (1997) 2810.
[91] R.J. Asaro, S. Suresh, Acta Mater. 53 (2005) 3369.
[92] Y.M. Wang, A.V. Hamza, E. Ma, Acta Mater. 54 (2005) 2715.
[93] M.S. Phen, R.T. Crosby, V. Craciun, K.S. Jones, M.E. Law, J.L. Hansen, A.N. Larsen, Mater. Res. Soc. Symp. Proc. 864 (2005) E4.28.1.
[94] W. Barvosa-Carter, M.J. Aziz, Mater. Res. Soc. Symp. Proc. 441 (1997) 75.
[95] W. Barvosa-Carter, M.J. Aziz, L.J. Gray, T. Kaplan, Phys. Rev. Lett. 81 (7) (1998) 1445.
[96] J.F. Sage, W. Barvosa-Carter, M.J. Aziz, Appl. Phys. Lett. 77 (4) (2000) 516.
[97] N.G. Rudawski, K.S. Jones, R. Gwilliam, Appl. Phys. Lett. 91 (17) (2007) 172103.
[98] R.G. Elliman, W.C. Wong, Appl. Phys. Lett. 69 (18) (1996).
[99] A.-V. Phan, T. Kaplan, L.J. Gray, D. Adelsteinsson, J.A. Sethian, W. Barvosa-Carter, M.J. Aziz, Modell. Simul. Mater. Sci. Eng. 9 (2001) 309.
[100] S. Morarka, N.G. Rudawski, M.E. Law, J. Vac. Sci. Technol. B 26 (1) (2008) 357.
[101] F.A. Cotton, G. Wilkinson, Advanced Inorganic Chemistry, Interscience, New York, 1972.
[102] J. Tersoff, A.W. Denier van der Gon, R.M. Tromp, Phys. Rev. Lett. 72 (2) (1994) 266.
[103] M. Reason, N.G. Rudawski, H.A. McKay, X. Weng, W. Ye, R.S. Goldman, J. Appl. Phys. 101 (2007) 083520.
[104] M. Li, J.W. Evans, Phys. Rev. B 73 (2006) 125434.
[105] W. Theis, R.M. Tromp, Phys. Rev. Lett. 76 (1996) 2770.
[106] O.P. Karpenko, S.M. Yalisove, D.J. Eaglesham, J. Appl. Phys. 82 (1997) 1157.
[107] F.C. Frank, J.H. van der Merwe, Proc. R. Soc. Lond. A 198 (1949) 205.
[108] M. Volmer, A. Weber, Z. Phys. Chem. 119 (1926) 277.
[109] I.N. Stranski, Von L. Krastanow, Akad. Wiss. Lit. Mainz Math. -Natur. K1 IIb 146 (1939) 797.
[110] D.J. Eaglesham, M. Cerullo, Phys. Rev. Lett. 64 (16) (1990) 1943.
[111] Y. Chen, J. Washburn, Phys. Rev. Lett. 77 (19) (1996) 4046.